JGR Solid Earth

RESEARCH ARTICLE
10.1029/2018JB016395

Microseismicity on Patches of Higher Compression During Larger-Scale Earthquake Nucleation in a Rate-and-State Fault Model

Natalie Schaal[1,2] **and Nadia Lapusta**[1,3]

[1]Department of Mechanical and Civil Engineering, California Institute of Technology, Pasadena, CA, USA, [2]Now at Department of Mechanical Engineering, Loyola Marymount University, Los Angeles, CA, USA, [3]Seismological Laboratory, California Institute of Technology, Pasadena, CA, USA

Abstract While many large earthquakes are preceded by observable foreshocks, the mechanism responsible for the occurrence of these smaller-scale seismic events remains uncertain. One physical explanation of foreshocks with growing support is that they are produced by the interaction of slow slip with fault heterogeneity. Inspired by the suggestion from laboratory experiments that foreshocks occur on fault asperities (bumps), we explore rate-and-state fault models with patches of higher normal stress embedded in a larger seismogenic region by conducting 3-D numerical simulations of their behavior over long-term sequences of aseismic and seismic slips. The models do produce smaller-scale seismicity during the aseismic nucleation of larger-scale seismic events. These smaller-scale events have reasonable stress drops, despite the highly elevated compression assigned to the source patches. We find that the two main factors contributing to the reasonable stress drops are the significant extent of the rupture into the region surrounding the patches and the aseismic stress release just prior to the seismic events. The smaller-scale seismicity can only occur if a sufficient separation in nucleation scales between the foreshock-like events and mainshocks is achieved. Our modeling provides insight into the conditions conducive for generating foreshocks on both natural and laboratory faults.

Key Points:
- Higher-compression patches can produce foreshock-like events due to nucleation-induced aseismic slip
- Such events have reasonable stress drops due to extended rupture area and aseismic stress release
- A sufficient separation in nucleation scales is needed for the occurrence of foreshock-like events

Correspondence to:
N. Schaal,
natalie.schaal@lmu.edu

Citation:
Schaal, N., & Lapusta, N. (2019). Microseismicity on patches of higher compression during larger-scale earthquake nucleation in a rate-and-state fault model. *Journal of Geophysical Research: Solid Earth*, *124*, 1962–1990. https://doi.org/10.1029/2018JB016395

Received 14 JUL 2018
Accepted 21 JAN 2019
Accepted article online 28 JAN 2019
Published online 18 FEB 2019

1. Introduction

Many large earthquakes are preceded by smaller seismic events, including foreshocks (Abercrombie & Mori, 1996; Bouchon et al., 2013, 2011; Bowman & King, 2001; Dodge et al., 1995, 1996; Doser, 1990; Jones & Molnar, 1976, 1979; Kato et al., 2012; Maeda, 1999; McGuire et al., 2005; Reasenberg, 1999; Zanzerkia et al., 2003), which are often interpreted to occur within the nucleating region of the mainshock. What mechanism is responsible for the occurrence of foreshocks? How are these precursory events able to occur in a nucleation region without immediately triggering the larger upcoming event? We seek to understand what conditions produce microseismicity within the nucleating region of the mainshock and to study the resulting events along with their properties through numerical modeling.

One viewpoint with growing evidence is that foreshocks are triggered by slow (aseismic) slip that interacts with fault heterogeneity (Bouchon et al., 2013; Brodsky & Lay, 2014; Dodge et al., 1995; Jones & Molnar, 1979; Kanamori & Stewart, 1978; Kato et al., 2012; Lengliné et al., 2012; Liu et al., 2007; Lohman & McGuire, 2007; McGuire et al., 2005; McLaskey & Kilgore, 2013; Segall et al., 2006). Dodge et al. (1996) determined that fault heterogeneity has an important influence both on the location of the nucleating region and the number of foreshocks. This is consistent with a broader view that much of microseismicity may be caused or facilitated by aseismic fault slip (e.g., Perfettini & Avouac, 2004, 2007; Wei et al., 2015). Heterogeneous fault properties could provide the means for smaller-scale seismic events to develop without perturbing the entire seismogenic (earthquake-prone) zone into a mainshock.

An important insight into this problem is provided by unique laboratory experiments of earthquake nucleation on a meter-scale slab of granite (McLaskey & Kilgore, 2013; McLaskey et al., 2014). The experiments produce quasi-static accelerating slip (nucleation process) that grows into dynamic rupture. Significantly, smaller seismically detectable events—foreshocks—occur in the nucleation region. The authors report that these small events, with magnitudes in the range of −7 to −5.5, typically have stress drops within the expected range for natural earthquakes (1–10 MPa). Due to persistent locations of the foreshock sources in

their repeated experiments, McLaskey and coauthors infer that these small seismic events are occurring at asperities, that is, bumps, on the fault interface. Fault nonplanarity is expected on natural faults (Brodsky et al., 2011; Candela et al., 2009; Renard et al., 2006; Sagy et al., 2007) and, when compressed into a full contact, would create places of highly elevated normal stress.

Inspired by these experiments, we explore the possibility of producing smaller-scale seismic events with reasonable stress drops during larger-scale aseismic nucleation slip in a rate-and-state fault model with patches of higher compression, with or without additionally increasing the smoothness of the patches (represented by a reduced characteristic slip distance). From their lab experiments, McLaskey and Kilgore (2013) infer a larger-scale nucleation size of about 1 m. They also infer that smaller events occur on patches with diameters on the order of 1 to 10 cm. Therefore, the model would need to incorporate two scales of nucleation sizes that are one to two orders of magnitude apart, which can be achieved by increasing the fault-normal stress correspondingly. While adding patches of higher normal stress to the seismogenic zone may seem like a straightforward way to perturb the larger-scale nucleation process into producing more complex behavior, at first glance, it is not expected to produce realistic behavior. In part, since shear stress on a frictional interface is proportional to the normal stress through a friction coefficient, one would assume that changes in shear stress would also be proportional to the normal stress, potentially leading to unrealistically high stress drops for the seismic events on patches with highly elevated normal stress.

We use a numerical approach (Lapusta & Liu, 2009) that allows us to study the behavior of these patches over long-term sequences of earthquakes and aseismic slip, focusing on models with microseismicity driven by larger-scale nucleation processes. While we are motivated by the phenomenon of foreshocks, we create a more generic model in which the higher-normal-stress patches interact with aseismic creep from the nucleation process of the mainshock. For clarity in the discussion of our results, we coin the term intershocks: microseismicity occurring between two mainshocks within the creeping, nucleating portions of the seismogenic zone. Foreshocks would thereby be a subset of intershocks, depending on the foreshock definition. Since all our simulated intershocks are driven by the surrounding creep within the seismogenic zone, their study is relevant to the process of generating foreshocks, no matter when or where in the interseismic period they occur.

2. Methodology

2.1. Rate-and-State Friction and Nucleation Size

The law governing the frictional resistance of the fault in our model is rate-and-state friction. Derived from laboratory experiments on rocks at slow slip rates, rate-and-state friction has had much success in reproducing many earthquake phenomena, including earthquake nucleation, postseismic slip, aftershocks, and repeating earthquakes (e.g., Chen & Lapusta, 2009; Dieterich, 2007; Jiang & Lapusta, 2017; Kaneko et al., 2016; Lui & Lapusta, 2016).

In the rate-and-state friction laws, the frictional shear strength is related to effective normal stress through a dependence on the slip rate and "state" of the interface instead of the constant coefficient from classical Coulomb friction. In particular, the form applied in this study is the widely-used Dieterich-Ruina rate-and-state law, for constant effective normal stress (Dieterich, 1979; Ruina, 1983):

$$\tau = \sigma \left(f_* + a \ln \left(\frac{V}{V_*} \right) + b \ln \left(\frac{V_* \theta}{L} \right) \right), \tag{1}$$

$$\dot{\theta} = 1 - \frac{V\theta}{L}, \tag{2}$$

where τ is the shear resistance, σ is the effective normal stress (normal stress minus pore pressure), V is the slip rate, θ is a variable representing the state of the interface in contact (in units of time), L is the characteristic slip distance, a and b are rate-and-state parameters of the order of 0.01, and f_* is the reference friction coefficient at the reference slip velocity V_*. For a constant slip velocity V, the state variable θ evolves to its steady-state (ss) value $\theta_{ss} = L/V$, transforming the shear resistance τ into its steady-state form, $\tau_{ss} = \left(f_* + (a-b) \ln \left(V/V_* \right) \right)$. The sign of the quantity $(a-b)$ has important implications for the frictional stability of the modeled interface through its rate dependence. If $(a-b) > 0$, then we have velocity-strengthening behavior in steady state, which means that the faster the interface slips, the higher the frictional resistance. If instead $(a-b) < 0$, then we have velocity-weakening behavior in steady state,

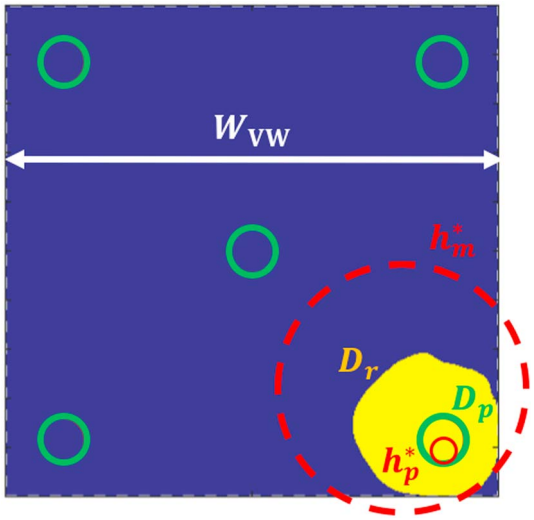

Figure 1. Schematic of important length scales in the problem for a given intershock: h_p^*, nucleation size of a patch with higher normal stress; D_p, diameter of the patch; D_r, diameter of ruptured area in a patch-initiated seismic event; h_m^*, nucleation size of the mainshock; and W_{VW}, size of the velocity-weakening region (seismogenic zone). For smaller-scale seismicity to occur on the patch, $D_p \geq h_p^*$ is generally needed. For the mainshock to occur, $W_{VW} > h_m^*$ is needed. In order for a patch-initiated seismic event to be reliably separated from the mainshock, D_r must be sufficiently separated from h_m^*, that is, $D_r \ll h_m^*$. Our simulations show that $D_p \ll D_r$ in many cases. Thus, satisfying the condition $h_p^* \leq D_p \ll D_r \ll h_m^* < W_{VW}$ enables the occurrence of many intershocks per mainshock.

meaning the frictional resistance decreases with increasing sliding velocity. While velocity-strengthening interfaces respond to slow tectonic loading with slow stable slip, velocity-weakening interfaces can produce spontaneously accelerating slip (i.e., an earthquake; Dieterich, 1992; Rice & Ruina, 1983; Rubin & Ampuero, 2005).

In order for an interface to transition into dynamic rupture, not only does the frictional dependence need to be velocity weakening but also the size of the nucleating region with these properties needs to be larger than the nucleation size h^* (Rice & Ruina, 1983; Rice et al., 2001; Rubin & Ampuero, 2005). Theoretical estimates for the nucleation size are generally based on stability analyses in homogeneous 2-D settings. We utilize the theoretical estimate $\tilde{h}^*_{RA}$, given by

$$\tilde{h}^*_{RA} = \frac{2}{\pi} \frac{\hat{\mu} b L}{(a-b)^2 \sigma}, \tag{3}$$

where $\hat{\mu} = \mu$ for mode III ruptures and $\hat{\mu} = \mu/(1-\nu)$ for mode II ruptures, μ is the shear modulus, and ν is Poisson's ratio. This estimate was derived by Rubin and Ampuero (2005) from a fracture energy balance analysis of a crack extending quasi-statically for the Dieterich-Ruina rate-and-state parameter regime of $a/b > 0.5$. For a fault in a 3-D elastic medium, the nucleation size estimate is expected to increase by a factor of 2 or 3; in particular, the 3-D estimate of

$$\tilde{h}^*_{3D} = \left(\pi^2/4\right) h^*_{RA}, \tag{4}$$

with $\hat{\mu} = \mu$ has been successful in matching the combined nucleation sizes produced by 3-D earthquake simulations (Chen & Lapusta, 2009), and it is the estimate used in this study. For clarity, we notate the theoretical nucleation size estimates, which are calculated directly from input model parameters, with a tilde, as in equations (3) and (4).

The ratio between the size of the seismogenic region (the velocity-weakening region in the rate-and-state framework) W_{VW} and the nucleation size h^* is a helpful indicator of how prone to instability a given fault is. A ratio of $W_{VW}/h^* < 1$ implies quasi-static behavior (no earthquakes), whereas a value greater than one predicts stick-slip behavior (Lapusta & Liu, 2009).

As the estimates show (e.g., equation (3)), the nucleation size depends on the effective normal stress and fault frictional properties. In addition, simulations show that there are other factors that can affect the nucleation size h^*, such as the loading rate (e.g., Kaneko & Lapusta, 2008; Lapusta et al., 2000). Furthermore, since the aforementioned $\tilde{h}^*$ estimates are for homogeneous faults, the appropriate treatment in a heterogeneous setting is an open question.

2.2. Length Scales in the Problem and Microseismicity Occurrence

With the goal of producing microseismicity within the nucleation region of the mainshock, we consider circular patches of higher compression within the seismogenic zone. In order for the dynamic ruptures on these patches to remain separated from the upcoming mainshock, a separation in length scales is needed (Figure 1). While these events may be interacting through stress changes, especially those induced by post-seismic slip, as discussed briefly in section 3.2, we occasionally refer to the seismic events as "separated" or "isolated" when the seismic events initiating on a smaller scale stop before rupturing the majority of the velocity-weakening domain as a mainshock.

To produce a seismic event on a patch, the patch diameter D_p needs to be comparable to or larger than the local nucleation size h_p^*. When the patch ruptures, our simulations show that the rupture extent of the intershock D_r is larger, and often much larger, than the patch diameter D_p (section 3.4). At the same time, D_r needs to be sufficiently smaller than the mainshock nucleation size h_m^* or else the patch rupture immediately triggers the mainshock, with no smaller-scale seismicity. Therefore, the nucleation size on the patch h_p^* and the mainshock nucleation size h_m^* need to be well separated according to

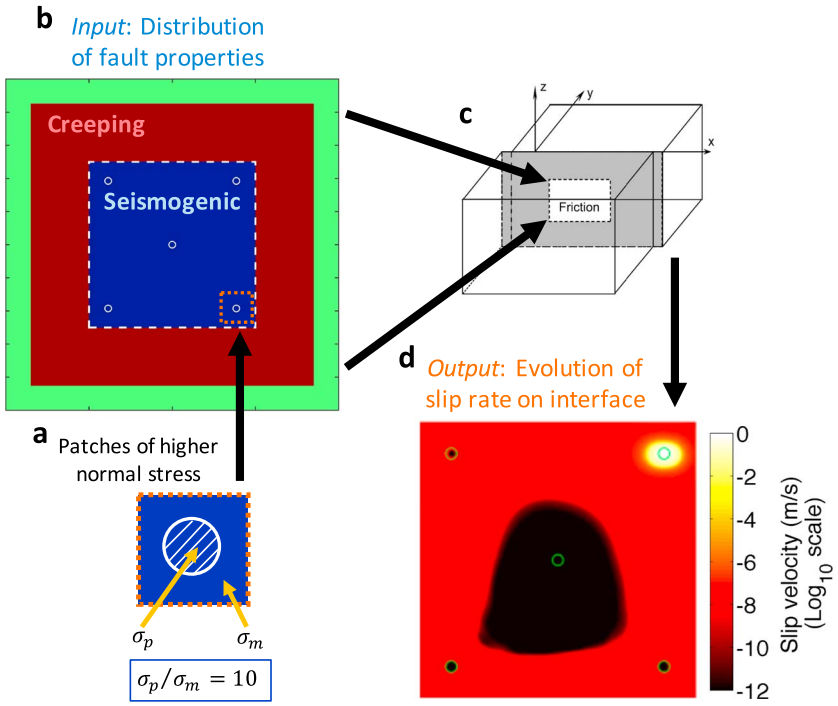

Figure 2. Schematic of the modeling process. (a) A typical circular patch of higher normal stress in our model. (b) The circular patches (5 in this case) are distributed within the seismogenic zone (blue), which is loaded by the surrounding creeping region (red) and transmits the plate-rate loading from the boundary region (green). (c) The 2-D heterogeneous fault is embedded in a 3-D homogeneous elastic bulk. Through fully dynamic calculations, the result of our simulations is the evolution of slip and stress on the fault. (d) An example snapshot of slip rate over the seismogenic region during a patch-hosted seismic event (upper right patch).

$$h_p^* \le D_p \ll D_r < h_m^*. \tag{5}$$

Furthermore, the mainshock nucleation size h_m^* must be smaller than the size of the velocity-weakening region W_{VW} for mainshocks to initiate in the background seismogenic region. This condition provides larger-scale seismic events in addition to the smaller-scale seismic events initiating on circular patches of higher normal stress σ_p, and its effect is discussed further in section 3.7. In addition, we separate the centers of the patches by approximately $\tilde{h}_m^*$ diagonally and approximately $1.5\tilde{h}_m^*$ in the vertical and horizontal directions so that the patches are close enough for the mainshock nucleation to involve the patches yet as distant as possible to ensure that the intershocks are separated from one another. Considering scenarios with more densely spaced patches that would rupture together or significantly interact is outside the scope of this work and remains an interesting problem for a future study.

2.3. Model Geometry and Parameters

Our fault model (Figure 2) is divided into three regions: a seismogenic (velocity-weakening) zone where earthquakes can happen, a stably creeping (velocity-strengthening) section, and a boundary region where a "plate rate" style loading is applied (Figure 2b). The velocity-strengthening region serves to transmit the slow loading to the initially locked seismogenic zone. The loading rate is chosen to approximately reproduce the average shear stress rate of 0.001 MPa/s on the fault, from the motivating work of McLaskey and Kilgore (2013).

In our models, both the circular patches and the surrounding seismogenic zone have the same velocity-weakening parameters a and b. This setup is in contrast to the more common approach of velocity-weakening patches embedded in a velocity-strengthening creeping region (e.g., Chen & Lapusta, 2009; Lui & Lapusta, 2016). There is an important difference between the two types of models: Dynamic ruptures on patches embedded in a velocity-strengthening region tend to arrest in the surrounding region unless enhanced dynamic weakening is present there (e.g., Noda & Lapusta, 2013), whereas in our model, both the patches and the immediate surrounding region can sustain dynamic slip, as they both are

velocity-weakening. The rate-and-state parameters a and b used in this study are on the order of 0.01, and the constant L_m on the background of the fault falls within the range of 1–100 microns, as in laboratory experiments on rock specimens (e.g., Dieterich, 2007; Dieterich & Kilgore, 1996; Marone, 1998).

Within the seismogenic zone, we place a grid of circular patches of higher normal stress (Figure 2a) to ensure that the mainshock nucleation would interact with some of the patches, regardless of where the nucleation originates. This grid-like placement of the patches is not meant to be indicative of the asperity distribution on natural or laboratory faults but instead provides a simplified geometry with well-spaced sources. The arrangement of our model allows us to explore smaller-scale seismic events within the extended nucleation region of the mainshock, driven by the mechanism of slow slip from the mainshock nucleation. While we explore a variety of patch properties for producing intershocks, the number and location of the patches are held constant.

Our goal is to study the resulting intershocks in detail, in order to understand the conditions under which they are produced and whether they have reasonable properties, including stress drops. To that end, we focus only on the nucleation phase of the mainshocks by making the entire seismogenic region only up to two times larger than the larger-scale nucleation size. Thus, our mainshocks end shortly after nucleating, making them relatively small, and we do not explore the details of their rupture propagation. In particular, our mainshocks are crack-like, in the sense that the local slip duration for most points on the fault is comparable to the overall duration of the event (e.g., Noda et al., 2009; Zheng & Rice, 1998). Some observations suggest that large events are pulse-like (Heaton, 1990), with local slip durations much shorter than the overall even duration; the transition between crack-like and pulse-like rupture modes may occur for events that are large enough, for example, Meier et al. (2016) conclude that the transition occurs around M_w 4.5. Studying such large events is beyond the scope of this work.

The circular patches within the seismogenic region are characterized by higher compression σ_p and/or lower characteristic slip L_p than the values σ_m and L_m for the surrounding (or main) seismogenic zone (Figures 3a and 3b). The higher normal stress σ_p represents more pronounced "bumps." After the two sides of the fault repeatedly slide past each other over many events, the more compressed patches may also become smoother, represented by a reduced characteristic slip distance L_p within our rate-and-state framework, as supported by experimental observations (e.g., Marone & Kilgore, 1993). Recalling the nucleation size estimate (equation (4)), both a higher value of normal stress σ_p and a reduced value of L_p contribute to a smaller local nucleation size on the patches h_p^*, leading to a separation in nucleation length scales that potentially allows for microseismicity. Given our focus on exploring patches of higher normal stress, whenever we additionally decrease L_p to help produce a smaller nucleation size, the L ratio L_p/L_m is 0.5. Thus, the main variable characteristics of our patches can be described by the following nondimensional parameters: normal stress ratio σ_p/σ_m.

The model parameters studied in this work are divided into two sets: the main set and the Variable Background Normal Stress (VBNS) set. The two sets share a number of properties, including the bulk material properties, the rate-and-state parameters, and the loading rate (Table 1). The central difference between these sets is that the models in the main set all have the same background normal stress σ_m, while the patch properties are varied (Table 2), and for the VBNS set, the patch properties are held constant, while the value of σ_m, and hence σ_p/σ_m, is varied (Table 3). Within the results presented here, three representative simulations from the main set are repeatedly highlighted. For ease of discussion, we call them cases A–C (Table 4). For further clarity in the presentation of results and discussions, a summary of the notations used is given in Table 5.

While the vast majority of the models studied here does result in intershocks, the few models that do not result in intershocks can provide insight into the bounds of this phenomenon. Two different scenarios for suppressing intershocks have emerged in the two sets of models presented here: (1) overly strong patches and (2) subseismic patches. In the first scenario, despite the patches having an instability ratio greater than one, the loading from the interseismic creep is not enough to reach the level of shear stress on the patch needed to cause high (seismic) slip rates before the upcoming mainshock begins in the surrounding area. In the instance where this occurs in our study, the normal stress ratio σ_p/σ_m is 15, and the patch instability ratio $D_p/\tilde{h}_p^*$ is 1.2 (purple filled-in triangle in Figure 3). Notably, two other models in our study also have $\sigma_p/\sigma_m = 15$, but they have different instability ratio and patch size, allowing for the occurrence of intershocks. The second scenario arises when the patches have too low of an instability ratio to host seismic

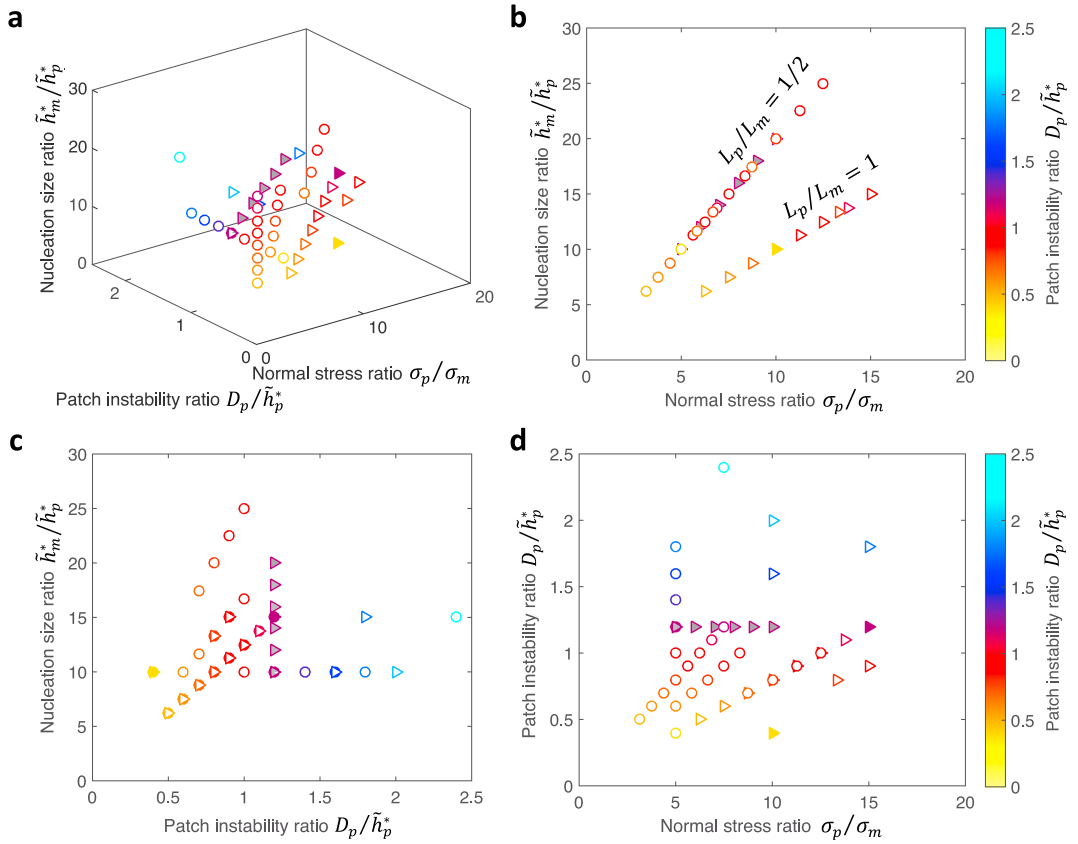

Figure 3. Characteristics of the patches used in this study. Each marker represents one model, while the outline color indicates how prone to dynamic instability the patches should be. Circular and triangular markers identify models with $L_p/L_m = 1/2$ and $L_p/L_m = 1$, respectively. Gray-filled markers indicate models from the Variable Background Normal Stress set (discussed in detail in section 3.6), which all produce intershocks. For the main set, markers filled with the same color as their outline color represent models that do not produce intershocks (i.e., only produce mainshocks), and white-filled markers indicate models that do produce intershocks and thereby satisfy the required separation of scales (equation (5)). (a) 3-D plot indicating the separation in nucleation sizes between the intershocks and mainshocks, instability ratio of the patches, and elevated normal stress on the patches, showing the span of properties explored in this study. (b) Since $\tilde{h}^*$ is proportional to σ and inversely proportional to L (equation (4)), the relationship between the separation in nucleation sizes and normal stress ratio falls into two distinct lines, one for each L_p/L_m. For the main set, since σ_m, L_m, and $\tilde{h}_m^*$ are held constant, the same $\tilde{h}_m^*/\tilde{h}_p^*$ can be achieved by doubling both L_p and σ_p. For the Variable Background Normal Stress set, since σ_p and $\tilde{h}_p^*$ are held constant, increases in $\tilde{h}_m^*$ via decreases in σ_m result in the same linearity between $\tilde{h}_m^*/\tilde{h}_p^*$ and σ_p/σ_m as for the main set. (c and d) The remaining distinct sides of the 3-D plot in (a).

events. Interestingly, this lower bound on instability ratio seems to also be dependent on the levels of normal stress and characteristic slip distance that establish the nucleation size on the patch and, hence, the patch instability ratio: For two models with $D_p/\tilde{h}_p^* = 0.4$ in our study, the one with $\sigma_p/\sigma_m = 10$ and $L_p/L_m = 1$ does not produce intershocks (yellow filled-in triangle in Figure 3), while the other case with $\sigma_p/\sigma_m = 5$ and $L_p/L_m = 1/2$ does produce some intershocks. In addition, recall that an insufficient separation of scales would also prevent intershocks from happening, for example, when a patch-initiated dynamic rupture grows large enough to reach the nucleation size of the mainshock (section 2.2). Clearly, the full description of the conditions for producing intershocks is complex. Note that, especially in cases with $D_p/\tilde{h}_p^* < 1$, a significant part of the nucleation occurs outside of the patch (section 3.2).

2.4. Numerical Approach and Resolution

We utilize the simulation methodology of Lapusta and Liu (2009), which enables the analysis of a 2-D planar fault enclosed in a 3-D homogeneous elastic bulk. It employs the Boundary Integral Method to accurately and efficiently model both the inertial effects during simulated earthquakes and slow slips during relatively long interseismic periods. To take advantage of the efficient Fourier representation of the Boundary Integral Method procedure (Lapusta & Liu, 2009), we consider an infinite interface created by a periodically repeated

Table 1
Parameters Shared by All Models

Parameter	Symbol	Value
Background characteristic slip distance	L_m	1 μm
Rate-and-state properties in VW region	a	0.0100
	b	0.0255
Reference friction coefficient	f_*	0.6
Reference slip velocity	V_*	10^{-6} m/s
Poisson's ratio	ν	0.25
Shear modulus	μ	30 GPa
S wave speed	c_s	3.0 km/s
P wave speed	c_p	5.2 km/s
"Plate" loading rate	V_{pl}	4.0×10^{-8} m/s

Note. "Background" refers to the values in the VW region outside of the patches, which are denoted by a subscript "m" for "main." VM = velocity weakening.

domain. In contrast to commonly used quasi-dynamic methods, which are often motivated by the reduction of computational cost from simplified handling of inertial effects during dynamic events (Rice, 1993), our simulation approach is fully dynamic. One critical element is the use of the variable time-stepping procedure from Lapusta et al. (2000), which chooses short time steps when the slip velocity is fast (dynamic rupture) and long time steps when the slip velocity is slow (interseismic period). Finally, the last critical element for solving these computationally demanding problems, due to the requirement of high spatial and temporal resolution to capture the dynamic effects over many loading cycles, is the use of parallel computing. All of these components combined allow us to simulate long-term fault behavior and to study microseismicity over many mainshock cycles.

The output of our simulations is the distribution in space and evolution in time of the slip on the fault. We consider the slip to be seismic if it occurs with the slip rate of 0.1 m/s or higher, which is a commonly used criterion that approximately captures the moment when the dynamic terms become important, following a line of work by other researchers (e.g., Bizzarri & Belardinelli, 2008; Lapusta & Liu, 2009; Noda & Lapusta, 2010; Rubin & Ampuero, 2005). Each seismic event begins and ends when the maximum slip rate on the fault becomes higher and lower, respectively, than 0.1 m/s. The earthquake moment is calculated by integrating slip at rates above 0.1 m/s over all fault cells that ruptured during the event (resulting in potency, with units of slip times area) and multiplying the result by the shear modulus. The rupture area is computed as the sum of all cells in which slip rate exceeds 0.1 m/s during the event. Based on prior studies, we expect the seismic slip rate threshold of 0.1 m/s to be reasonable and results for smaller thresholds to be similar, because the amounts of additional seismic slip and rupture area with the lower threshold values would increase only modestly. More detailed quantification of the effects of the assumed seismic threshold and the relation between the on-source thresholds and the observable seismic signals is a direction of our current work.

Table 2
Parameters in the Main Set

Parameter	Symbol	Value
Estimated background instability ratio	$W_{\mathrm{VW}}/\tilde{h}^*_m$	2
Background normal stress	σ_m	10 MPa
Diameter of patch	D_p	2–10 cm
Normal stress ratio	σ_p/σ_m	3.13–15.00
Characteristic slip distance on patch	L_p	0.5 or 1.0 μm
Estimated patch instability ratio	$D_p/\tilde{h}^*_p$	0.4–2.4
Estimated ratio of background nucleation size to patch nucleation size	$\tilde{h}^*_m/\tilde{h}^*_p$	6–25

Table 3
Parameters in the Variable Background Normal Stress Set

Parameter	Symbol	Value
Estimated background instability ratio	$W_{VW}/\tilde{h}^*_m$	1–2
Background normal stress	σ_m	5–10 MPa
Diameter of patch	D_p	6 cm
Normal stress ratio	σ_p/σ_m	5–10
Characteristic slip distance on patch	L_p	0.5 μm
Estimated patch instability ratio	$D_p/\tilde{h}^*_p$	1.2
Estimated ratio of background nucleation size to patch nucleation size	$\tilde{h}^*_m/\tilde{h}^*_p$	10–20
Estimated background nucleation size	$\tilde{h}^*_m$	0.5–1.0 m
Normal stress on patch	σ_p	50 MPa

The stage of fault behavior that is most numerically challenging is dynamic rupture, and the corresponding controlling parameter of the numerical resolution is the cohesive zone size (Day et al., 2005; Lapusta & Liu, 2009). This important parameter is defined as the spatial length scale over which the shear stress at the propagating rupture front drops from its peak to its residual value. Day et al. (2005) established that the initial cohesive zone size needs to be discretized by at least three to five spatial cells in order for dynamic rupture to be resolved. Since the patches in our simulations have an increased normal stress (which reduces the cohesive zone size), dynamic rupture on these patches is numerically costly, and so we restrict our patch normal stress to be up to 15 times higher than the background value.

Since we simulate the long-term behavior of the fault, the assigned initial conditions at the start of the simulation are not of particular importance. Instead, the prestress conditions for an event in the sequence are formed by the stress distribution created by the loading and prior fault slip.

3. Results

3.1. Sequences of Seismic Events

In the reference case of a homogeneous seismogenic zone, our simulations produce periodic sequences of events that span the velocity-weakening region and settle into a regular recurrence interval (Figure 4a); we refer to these events as mainshocks. In contrast, when we create heterogeneous faults by adding the circular patches of higher normal stress, the sequences of events become complicated (Figures 4b and 4c). Now both mainshocks and intershocks occur, with the intershocks sometimes occurring closely before, closely after, or far between the mainshocks. This irregular pattern persists, despite the fact that all of the five patches in a given model share the same properties (D_p, σ_p, L_p, a, and b). With the focus of our parameter regime on patches with significantly higher normal stress σ_p than the background σ_m, we often do not observe repeating intershocks occurring on the same patch within the same interseismic period of the mainshock. Based on a separate preliminary study (Schaal, 2018, Appendix A.2), we expect that the repeaters can be created by further reducing the characteristic slip distance L.

The heterogeneity in slip and shear stress created by the rupturing of these patches contributes to the complexity in the mainshock sequences as well. Although we do not focus here on how the occurrence of intershocks, which may be considered to be by-products of the mainshocks nucleation process, affects the mainshock nucleation process, the two heterogeneous fault cases shown here (Figures 4b and 4c) provide examples of this effect. Consider the case in Figure 4c.i, for example: Even though the patches of higher

Table 4
Highlighted Models From the Main Set

Model name	$D_p/\tilde{h}^*_p$	σ_p/σ_m	L_p/L_m	$\tilde{h}^*_m/\tilde{h}^*_p$
Case A	0.8	10.0	1	10
Case B	1.8	5.0	1/2	10
Case C	2.4	7.5	1/2	15

Table 5
Summary of Notations Used

Symbols	Parameters and variables
A_p, A_r	Patch and rupture areas
a, b	Rate-and-state parameters (equation (1))
c_s, c_p	S wave and P wave speeds
D_p, D_r, r	Patch diameter, effective diameter, and effective radius of rupture
D_r/D_p	Relative rupture extent
$D_p/\tilde{h}_p^*$	Estimated patch instability ratio
f_*, V_*	Reference friction coefficient and slip velocity
h^*, h_p^*, h_m^*	Actual nucleation size and its values on patches and in background
$\tilde{h}^*, \tilde{h}_{\mathrm{RA}}^*, \tilde{h}_{\mathrm{3D}}^*$	Nucleation size estimate and its values from Rubin and Ampuero (2005; equation (3)) and 3-D consideration (equation (4))
$\tilde{h}_p^*, \tilde{h}_m^*$	Estimated nucleation size on patches and in background
$h_m^*/D_r, \tilde{h}_m^*/D_r$	Actual and estimated isolation ratio
L, L_p, L_m	Characteristic slip and its values on patches and in background
M_0, M_w	Seismic moment and moment magnitude
t_{r}	Mainshock recurrence time
V, V_{pl}	Slip velocity and "plate" loading rate
W_{VW}	Size of the seismogenic region
$W_{\mathrm{VW}}/h_m^*, W_{\mathrm{VW}}/\tilde{h}_m^*$	Actual and estimated background instability ratio
γ, η_p, η_m	Constants from the simplified stress drop analysis of section 3.6
θ, θ_{ss}	State variable and its steady-state value
$\mu, \hat{\mu}, \nu$	Shear modulus, its generalization to include modes II and III, and Poisson's ratio
$\sigma, \sigma_p, \sigma_m$	Effective normal stress and its values on patches and in background
σ_p/σ_m	Normal stress ratio
τ, τ_{ss}	Shear stress and its steady-state value
$\bar{\Delta\tau}^{\mathrm{SD}}, \bar{\Delta\tau}_a$	Moment-based (equation (6)) and area-based stress drops (equation (7))
$\bar{\Delta\tau}_p, \bar{\Delta\tau}_m$	Average shear stress change on and outside of the patch (equation (7))
$\bar{\Delta\tau}_{\mathrm{total}}$	Total average shear stress change on the patch (seismic + aseismic)

normal stress should make the fault stronger overall, the mainshocks systematically happen earlier than in the homogeneous case (Figure 4a), corresponding to an average reduction in recurrence time of 10% per cycle (calculated over 10 mainshocks). Therefore, despite effectively adding "nails" to the seismogenic zone, the recurrence time of the mainshock decreases. This counterintuitive result is likely due to an accelerated nucleation process, which could be facilitated by one or a combination of the following factors: accelerated postseismic slip from the previous intershocks providing increased loading, one of the foreshock-like events growing into a mainshock, a smaller amount of slip per mainshock, or other factors. These effects would be interesting to investigate further in future work.

The chosen patch properties in a given model determine the frequency of intershock occurrence. In case A (Figure 4b), typically two intershocks occur per mainshock cycle, whereas in a case with the same instability ratio but smaller patches, lower normal stress, and lower characteristic slip (Figure 4c), six intershocks per cycle is typical. The last cycle in Figure 4c.i is expanded in Figures 4c.ii and 4c.iii to provide an example of how the occurrence of intershocks tends to increase in the latter half of the interseismic period of the mainshock and to highlight the intershocks occurring just before the upcoming mainshock. Based on their timing, these intershocks are the most foreshock-like. Note, however, that the entire sequence of intershocks is foreshock-like, in the sense that these events are triggered by the slow aseismic nucleation of the following larger dynamic event. Since the overall velocity-weakening domain is only double the larger-scale nucleation size, most of the interseismic period is also the nucleation period for the upcoming larger event.

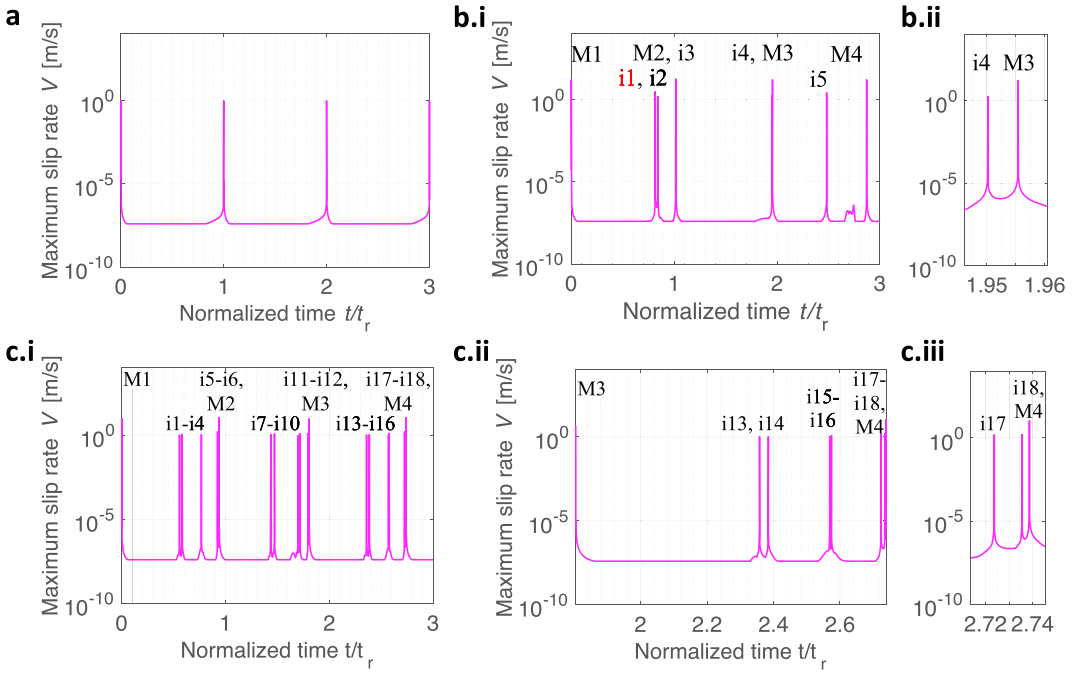

Figure 4. Maximum slip rate over the fault as a function of time. Flat sections correspond to the loading velocity of 4×10^{-8} m/s, and velocity spikes of the order of 10^0 m/s are seismic events. (a) The case of a homogeneous seismogenic region (i.e., no patches). (b.i) The heterogeneous fault of case A. (c.i) A heterogeneous fault with the same instability ratio of case A, except with $L_p/L_m = 1/2$ and $\sigma_p/\sigma_m = 6.66$. For all subplots, $t = 0$ corresponds to the fifth mainshock in the simulation, and the time axes are normalized by the average recurrence time t_r of the homogeneous case. Seismic events are labeled, where "M#" and "i#" enumerate mainshocks and intershocks, respectively. (b.ii) Expanded snippet of (b.i) to show how closely i4 happens before M3 (time separation is approximately 0.5% of t_r). (c.ii) Events for the last mainshock cycle shown in (c.i). (c.iii) Expanded snippet of (c.ii) to highlight two intershocks that occurred closely before M4 (time separation between i17 and M4 and i18 and M4 was approximately 1.5% and 0.3% of t_r, respectively). Event i1 in (b.i) labeled in red is analyzed in more detail in Figure 6.

To visualize a representative interseismic period between mainshocks, Figure 5 shows snapshots of the spatial distribution of slip velocity from the event sequence in Figure 4b. At the start of this sequence of snapshots, the seismogenic region is locked (Figure 5a). As the aseismic slip develops in the velocity-weakening region and interacts with the patches, an intershock occurs at the upper right patch (Figure 5b) and results in postseismic slip (Figure 5c). Another intershock and its resulting postseismic slip occur soon thereafter (Figures 5d and 5e). Finally, a mainshock nucleates in the upper right quadrant (Figure 5f) and proceeds to rupture the entire seismogenic region. These examples (Figures 4 and 5) show that our simulated fault behavior has the qualitative features that we set out to achieve, namely, the occurrence of smaller-scale seismic events within the aseismic slip of the continued nucleation process of the upcoming larger-scale event.

The classification choice of mainshock or intershock for most of the seismic events discussed in this work is obvious (e.g., events in Figure 5). However, in some cases, the rupture complexity produces less of a distinction between the two groups, with dynamic events rupturing most but not all of the velocity-weakening region. For clarity and consistency in the discussion of our simulation results (e.g., for designating the relative rupture extent D_r/D_p in section 3.4), we define the intershocks to be patch-initiated events that either partially or completely rupture a single patch of elevated normal stress and have a rupture area that is less than two thirds of the total area of the seismogenic zone. Mainshocks are larger-scale events that often rupture the entire velocity-weakening region, serving to reset the loading cycle. Our mainshocks are not much larger than their nucleation size, only by a factor of about 2, for computational efficiency. In other words, our model is designed to simulate the nucleation process that interacts with stronger fault patches, produce some intershocks, allow the larger-scale nucleation to accelerate to dynamic slip, and then to arrest the larger-scale event soon afterward. As such, our "mainshocks" are not the focus of this study, and we do not analyze them in depth here.

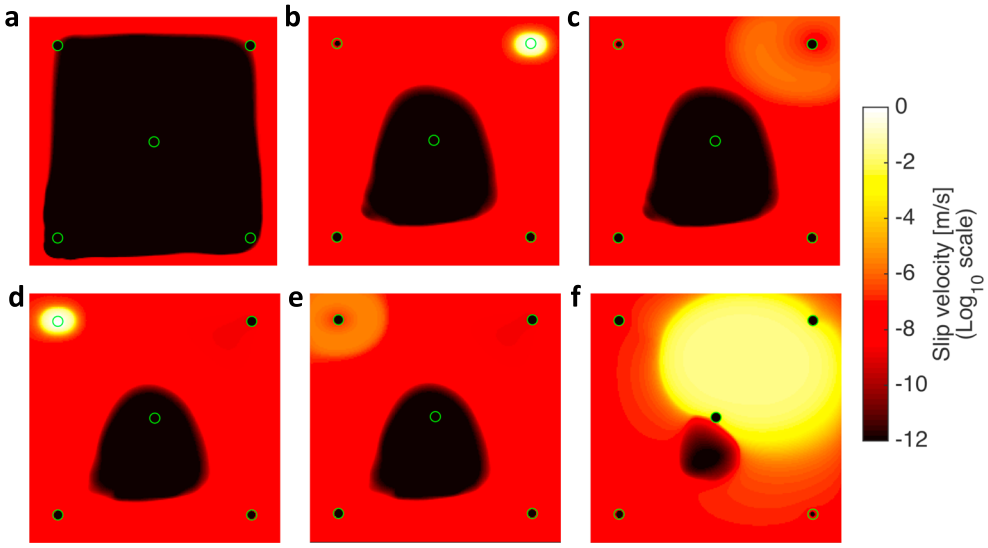

Figure 5. Snapshots of the slip velocity distribution over the seismogenic region for case A, with the five circular patches outlined in green. On this log scale, bright yellow and white correspond to seismic slip rates, orange and red correspond to aseismic slip, and black indicates regions that are effectively locked. The panels capture the interseismic creep before event M2 in Figure 4b that includes two intershocks (i1 and i2). (a) Early interseismic period. (b and c) Intershock i1 and the associated postseismic slip. (d and e) Intershock i2 and its postseismic slip. (f) Late stages of the nucleation of mainshock M2.

The plethora of data provided by our numerical simulations allows us to study the details of how the patches of higher normal stress are loaded by the surrounding aseismic creep and rupture in a dynamic event (Figure 6). The evolution of an intershock on a patch can be illustrated by four quantities from our simulations: the logarithm of the slip velocity $\log_{10}(V)$, the slip velocity V itself, the effective friction coefficient τ/σ, and the shear stress τ (rows A–D in Figure 6). The logarithm of the slip velocity highlights the acceleration of slip as the intershock nucleates but blurs the details in the seismic slip velocity distribution. Snapshots directly of the slip velocity, on the other hand, show the progression of the seismic rupture (seismic slip rates are shown as all colors other than orange in row B of Figure 6). The effective friction coefficient, which is the shear stress normalized by the normal stress, emphasizes the shear stress change outside of the patch. Lastly, snapshots directly of the shear stress detail the buildup and lowering of shear stress on the patch.

In the nucleation process of an intershock, the patch starts locked (Figure 6A1) until aseismic slip due to the larger-scale nucleation process around the patch engulfs it (Figure 6A2), accelerating the slip rates through the start of the seismic event (Figure 6B4). From this point on, the slip rates continue to rise as the event ruptures the patch and extends into the surrounding region (Figures 6B5–6B9) until the event dies out (Figure 6B10). Additionally, comparing the slip rate and shear stress in a period prior to the start of the seismic event reveals that the shear stress builds up to a peak and then drops slowly until the event starts (Figures 6D1–6D4), while the slip rates were below the seismic threshold and seemingly stagnant (Figures 6B1–6B4). This aseismic stress release just before the seismic event occurs within the nucleation zone of the patch, which occupies most of the patch in this particular case, and would likely be difficult to detect on natural faults. However, it can be explored via numerical simulations and is discussed further in section 3.5. The surprisingly large extent of the rupture into the region outside of the patch is also discussed further, in section 3.4.

3.2. Nucleation of Intershocks

In order for a seismogenic (velocity-weakening) region to produce a dynamic event, the region must be larger than its corresponding nucleation size h^* (section 2.1). To determine the potential for a given zone to produce seismic events, the nucleation size can be estimated based on theoretical considerations, for example, equations (3) and (4). While this estimate is derived for a seismogenic region with homogeneous properties, the case of our simulations is much different, as we model the 3-D problem with a seismogenic region that has heterogeneous normal stress and occasionally heterogeneous characteristic slip distance.

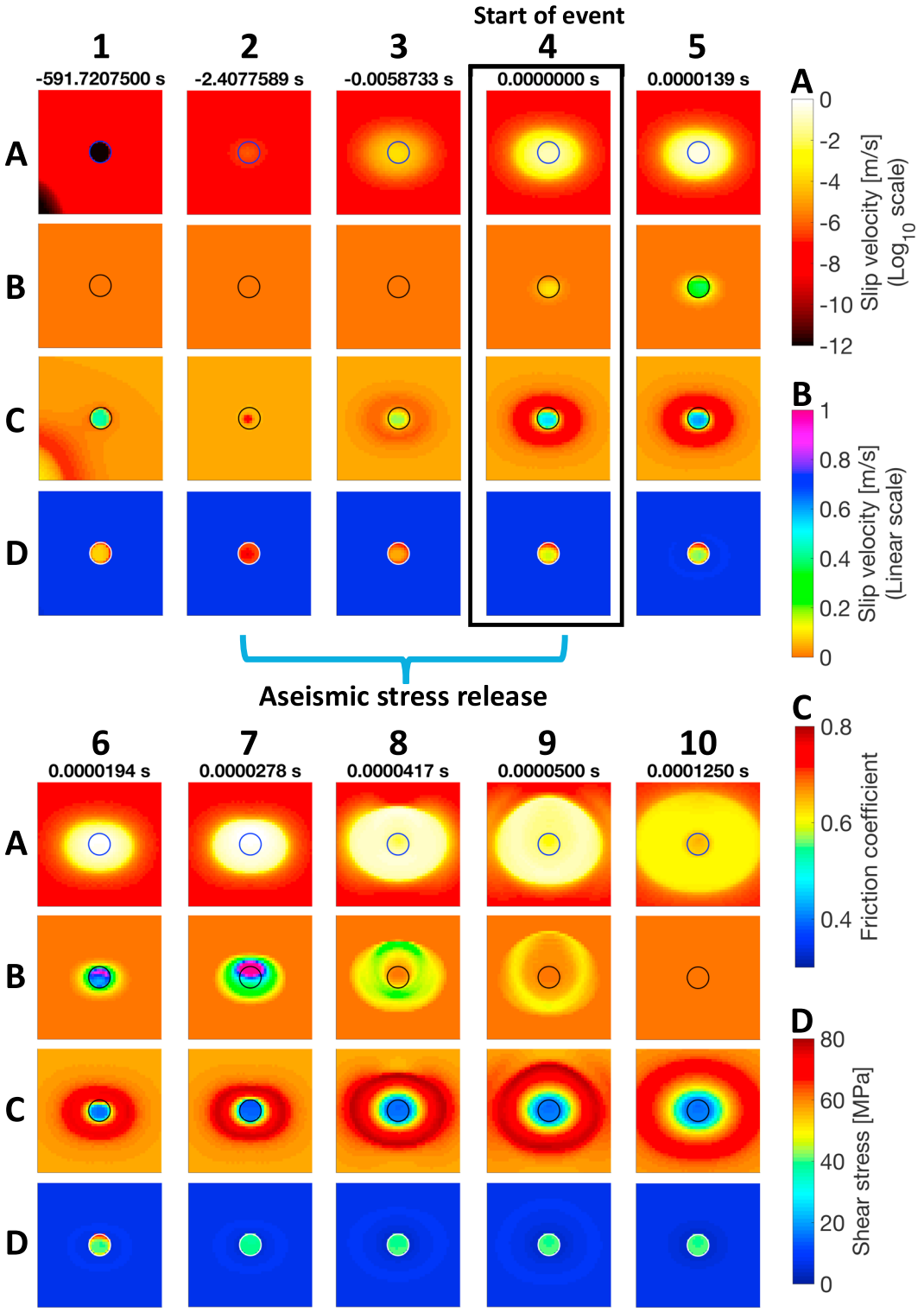

Figure 6. Snapshots of slip velocity (rows A and B), friction coefficient (row C), and shear stress (row D) evolution for an intershock (event i1 from Figure 4b.i, i.e., case A). The color scale of row A is the same as in Figure 5, and the color scale for row B highlights the seismic slip velocity comparable to the threshold of 0.1 m/s (yellow). The time relative to the start of the intershock (in seconds) is displayed above each column of snapshots, with a black box highlighting the column corresponding to the event start.

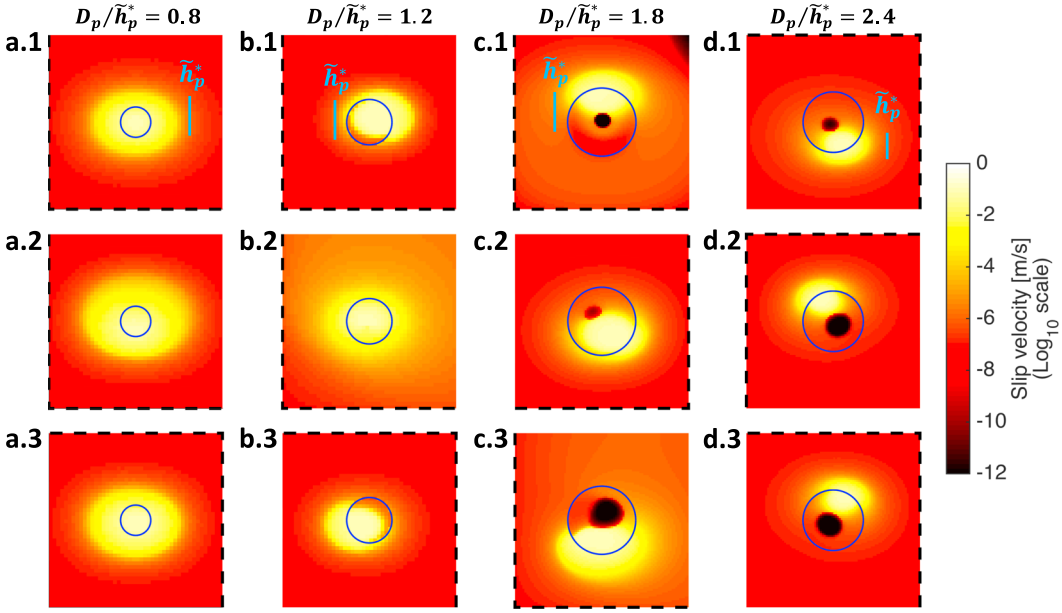

Figure 7. Snapshots of slip velocity at the end of the nucleation process of twelve different intershocks. The columns (a)–(d) correspond to four models with different patch properties, and the rows (1)–(3) show different intershocks from the same simulation. The color scale is the same as in Figure 5. (a) Case A. The completed nucleation for all of the events in this simulation looks similar. (b) Same properties as case B except $D_p/\tilde{h}_p^* = 1.2$. Nucleation shapes b.1 and b.3 are typical for this model, whereas b.2 is the only one of its kind. (c) Case B. The three examples given highlight the variation in nucleation shapes for this model. (d) Case C. Nucleation d.1, with a smaller locked region, is the only one of its kind, as the nucleation for the rest of the events looks like d.2 and d.3. For the events in columns (a) and (b), there are no locked areas as the nucleation completes, whereas in columns (c) and (d) part of the patch is still locked. Note that the nucleation size estimate $\tilde{h}_p^*$ for each model is shown by a blue bar, and the boundary between the velocity-weakening and velocity-strengthening region is indicated by black dashed lines.

Since the effect of heterogeneity on nucleation size is not rigorously known, we set up our suites of model parameters based on the nucleation size from equation (4). For clarity, to indicate that this is an estimate for the nucleation size and that it is calculated from the model parameters prior to running the simulation, we notate it with a tilde, as $\tilde{h}^*$. Correspondingly, the tilde is omitted when we refer to the actual nucleation size, h^*.

Snapshots of the logarithm of the slip velocity V distributed on and around the patch at the moment when the seismic event starts illuminate how the intershocks in our models nucleate (Figure 7). It is apparent that events nucleating on a patch typically involve area adjacent to the patch in the nucleation as well (bright yellow regions in all events included in Figure 7). This behavior allows for the initially unexpected result that patches with $D_p/\tilde{h}_p^* < 1$ can still produce seismic events (e.g., events from case A in Figures 7a.1–7a.3). In addition, understanding how the patch properties translate into nucleation behavior is further complicated by the observation that features of the nucleation at the time it completes—for example, the proportion of the nucleating area within the patch, the amount of the patch that is locked, and the speed of the creep outside of the patch—vary for different events within the same simulation (e.g., Figures 7c.1–7c.3).

Some of the variability in the intershock nucleation within the same simulation can be attributed to the interaction between events via postseismic slip. A particularly clear example of one intershock influencing the upcoming intershock in this way is shown in Figure 8. In this example, the first intershock nucleates with accelerated slip over nearly the entire patch as the nucleation completes, as expected for its instability ratio of $D_p/\tilde{h}_p^* = 1.6$ (Figure 8c.1). The second intershock, on the other hand, begins when a significant part of the patch is still locked (Figure 8h.1). Analyzing a sequence of slip velocity snapshots (with the scale cropped to highlight creeping speeds) shows that the postseismic slip of the first event travels over to a neighboring patch, causing it to rupture sooner (Figures 8e–8h). This postseismic perturbation from the previous event allows the second patch to complete its nucleation early, with an apparently smaller nucleation size. The notion of smaller nucleation size with increased loading is in line with the findings of Lapusta et al. (2000) and Kaneko and Lapusta (2008). In addition, the long-range triggering of events through postseismic slip

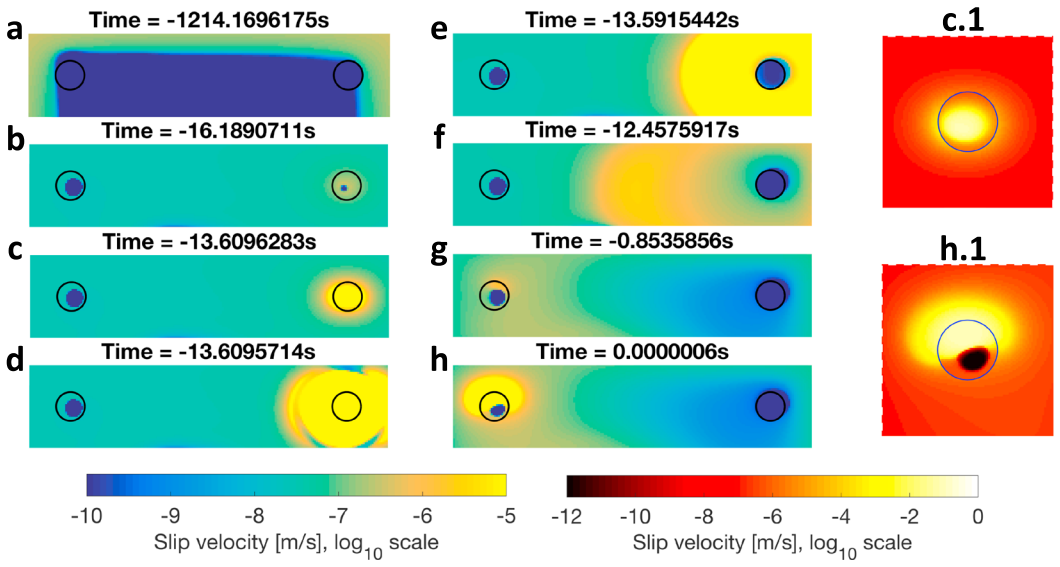

Figure 8. Long-range triggering between intershocks via postseismic slip and resulting variability in intershock nucleation. Postseismic slip from the first intershock (right patch) travels a distance of 8.6 patch diameters between the two and accelerates the nucleation of the second intershock (left patch). (a)–(h) Slip velocity on a log scale for a simulation with the same properties as case B, except $D_p/\tilde{h}_p^* = 1.6$: (a) early interseismic period; (b)–(d) intershock nucleation and rupture at the right patch; (e)–(g) resulting postseismic slip traveling to the left patch; (h) triggered intershock nucleation of the left patch. The color scale for snapshots (a)–(h) is cropped to highlight the postseismic front, and the spatial domain shown is restricted to a strip of the seismogenic zone. Time in seconds is given above each snapshot, relative to the start time of the event in (h). (c.1) Nucleation snapshot associated with the intershock in (c) (analogous to panels in Figure 7). (h.1) Same for the intershock in (h). While (c.1) exemplifies regular intershock nucleation for this simulation, (h.1) shows how the accelerated loading from the postseismic slip of the first intershock allows the second intershock to nucleate earlier and with a smaller nucleation size, leaving the center of the patch locked. The patches of higher normal stress in panels (a)–(h) and (c.1) and (h.1) are outlined in black and blue, respectively.

is consistent with the findings in Lui and Lapusta (2016) that neighboring repeating earthquakes interact primarily via postseismic slip and over larger distances than previously assumed.

To gain a more accurate sense of the nucleation sizes for the intershocks in our models, it would be useful to measure the nucleation size directly from the simulation results, but the procedure for how to do so is not obvious. Previous studies have shown that the nucleation estimates developed thus far work well for the more typical scenario of a velocity-weakening patch surrounded by a velocity-strengthening region (e.g., Chen & Lapusta, 2009). In that case, the achieved nucleation size is also easier to measure because the falloff of slip rates is much sharper, resulting in more clearly defined edges of the nucleation than in our scenario, where both the patches and surrounding seismogenic region are velocity-weakening and accelerating toward failure, albeit on different time scales. In our case, the nucleated area extends outside of the patch, where the properties and thereby the nucleation size is much different ($\tilde{h}_m^*$ is usually 10 or more times larger than $\tilde{h}_p^*$ in our models), and the question remains of how to combine the nucleation length scales measured on and off the patch into a unifying nucleation size estimate. Furthermore, since the nucleation sizes in the modes II and III directions differ by a factor of $1/(1-\nu)$, we have an orientation problem in 3-D, unless the nucleated area is perfectly elliptical and lined up with the modes II and III slip directions.

Given these uncertainties and variability, we measure a reference length scale for the nucleation size as the largest dimension of the nucleated area in the radial direction within the circular patch, from the log scale slip rate snapshots at the moment, the seismic slip rate threshold of 0.1 m/s is reached (defined as the start of the dynamic event). These "nucleation size" measurements typically range from 65% to 100% of the formulaic nucleation size estimate $\tilde{h}_p^*$ (from equation (4)), with values over 100% being unusual; therefore, our patches are more unstable than initially estimated, likely due to part of the nucleation being accommodated by the surrounding background region. A more comprehensive nucleation size calculation would require a weighted combination of the nucleation extents on and off the patch or perhaps a linear dimension computed from the total nucleating area.

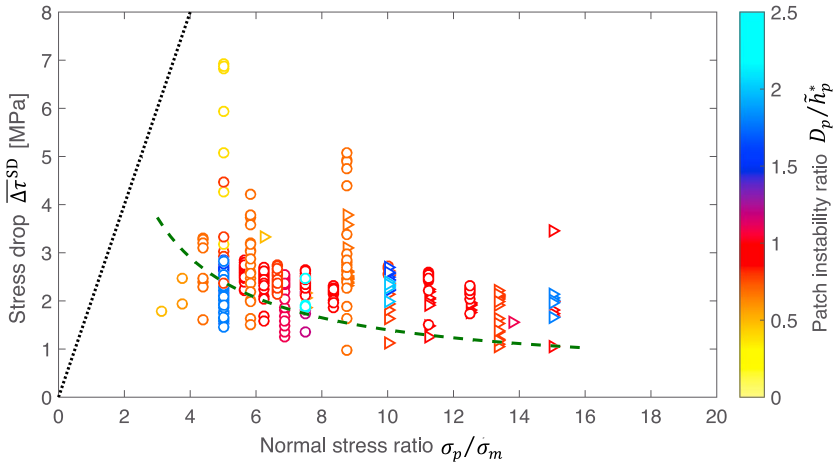

Figure 9. Stress drops of intershocks as a function of the patch normal stress. For this set of models, the background properties (σ_m, L_m, a, and b) are kept constant, and each simulation is run for the same simulated time, which typically produces 10 mainshocks cycles. Each marker represents an intershock, while each combination of outline color, marker type, and normal stress ratio σ_p/σ_m identifies a model. The outline color indicates the instability ratio of the patch $D_p/\tilde{h}_p^*$, with respect to the nucleation size estimate $\tilde{h}_p^*$ (equation (4)). Circular markers indicate $L_p/L_m = 1/2$, whereas triangular markers indicate $L_p/L_m = 1$. The vertical spread in markers with the same identifying properties shows the range of stress drops observed for a given simulation with multiple intershocks. The black dotted line and the green dashed line show the approximate expected trend of $\bar{\Delta\tau}^{SD} = 0.2\sigma_p$ and the simplified stress drop calculation ($\bar{\Delta\tau}_a^{SD}$, equation (10)), respectively. The stress drops of the intershocks in our models are in the reasonable range of about 1–7 MPa and approximately constant, despite the range of variation in the patch normal stress.

3.3. Stress Drops of Intershocks

Sections 3.1 and 3.2 jointly provide examples of intershocks that have successfully nucleated on the circular patches of higher compression within the seismogenic zone. However, the question remains: do these smaller-scale seismic events have realistic stress drops in the range of what is observed? Based on the proportionality between the shear stress and normal stress through the friction coefficient, one would expect the stress drops to scale linearly with the normal stress and hence expect unreasonably high stress drops for the seismic events initiating on the patches of highly elevated normal stress. Calculating the slope for the expected trend in stress drops versus normal stress using the average mainshock stress drop from the 10 mainshocks in the homogeneous fault simulation (shown in Figure 4a) divided by the background normal stress σ_m yields 0.20 for our main set of simulations.

Unexpectedly, our simulations show that the intershocks have near-constant stress drops, nearly independent from the patch normal stress, for a wide range of patch parameters (Figure 9). The computed stress drops have reasonable values, consistent with the typical range of 1–10 MPa from the lab (McLaskey et al., 2014) and the field (Abercrombie, 1995). We compute the stress drops $\bar{\Delta\tau}^{SD}$ for the simulated events from their seismic moment M_0 and effective rupture radius $r = \sqrt{A_r/\pi}$, where A_r is the rupture area, using the standard expression for a circular crack model (Eshelby, 1957; Kanamori & Anderson, 1975):

$$\bar{\Delta\tau}^{SD} = \frac{7}{16}\frac{M_0}{r^3}. \tag{6}$$

Note that the superscript "SD" here refers to the "stress drop," which is a positive quantity that represents the average difference in the shear stress before and after the event. The stress drops are computed using quantities estimated directly from our on-fault distributions and, in that sense, correspond to the actual (meaning an on-fault quantity instead of one inferred at a distance) stress drops.

The two simulations with the widest spread in the stress drops in Figure 9 (yellow and orange circles with $\sigma_p/\sigma_m = 5.00$ and 8.75, respectively) have low instability ratios, resulting in events that just barely qualify as seismic, that is, reach the slip rate threshold of 0.1 m/s. This spread may indicate a sensitivity of the rupture area to the chosen seismic velocity threshold for these barely seismic events.

The stress drop value, given by equation (6), is equivalent to a weighted average of the shear stress change over the entire seismically ruptured area. As can be seen from plotting the shear stress change over the fault

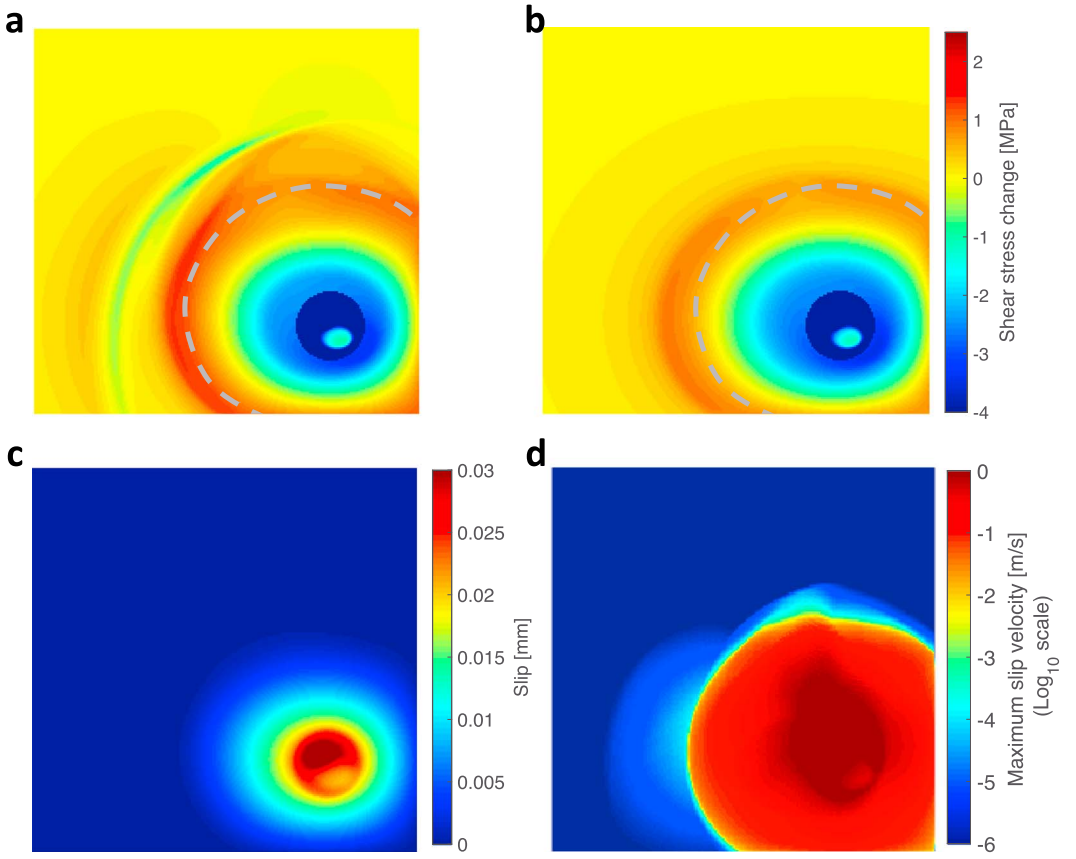

Figure 10. Example of shear stress change, slip, and maximum slip velocity for an intershock. (a) Spatial distribution of shear stress change due to seismic slip for an intershock from case B. The plot is spatially cropped to one quarter of the seismogenic region, and the color scale is chosen to highlight the stress changes outside of the patch. Blues and greens show decreased stress, yellow corresponds to near-zero stress changes, and reds and oranges show increased stress. The patch with elevated normal stress is shown by the mostly dark blue saturated circle. The approximate rupture extent for this event is outlined by the gray dashed line, defined by the area that reaches or exceeds the seismic velocity threshold of 0.1 m/s. (b) The same event, color scale, and dashed rupture line as in (a), but the shear stress change is computed using the stress distribution at the time after the event when the seismic waves have left the area. The additional time that has elapsed for (b) compared to (a) is approximately 1.8 times the intershock duration and incorporates the effects of initial postseismic slip. (c) Slip distribution corresponding to (a). (d) Maximum slip rate during the intershock on a log scale. The color scale range highlights the falloff in slip rates near the edge of the rupture.

for an intershock (Figures 10a and 10b), the shear stress change over the ruptured area is quite heterogeneous, with most of the significant decrease in stress occurring within a close neighborhood in and around the patch. (Note that, in Figure 10, we plot stress changes in a more traditional sense: final values minus initial values, which makes negative stress changes correspond to positive stress drops.) In addition, there is some stress increase within the ruptured area, near where the rupture arrests. These distributed stress changes are combined as a weighted average into the stress drop $\bar{\Delta\tau}^{SD}$ of equation (6). As proven in the work of Madariaga (1979), the moment-based stress drop $\bar{\Delta\tau}^{SD}$, which is commonly estimated from observations for small seismic events, represents the average of the stress drop distribution weighted by the final slip distribution of a constant-stress-drop source model.

The next two sections, 3.4 and 3.5, explore the key factors that lead to the unexpectedly reasonable and approximately normal-stress-independent stress drops, namely, the extended rupture area of the intershocks and the aseismic stress release on the patches (Higgins & Lapusta, 2017). Then, in section 3.6, we propose a simplified model for estimating the stress drops of intershocks based on reasoning about the seismic stress changes on and off the patch (Figure 11), along with parameters derived from the trends in our simulation results.

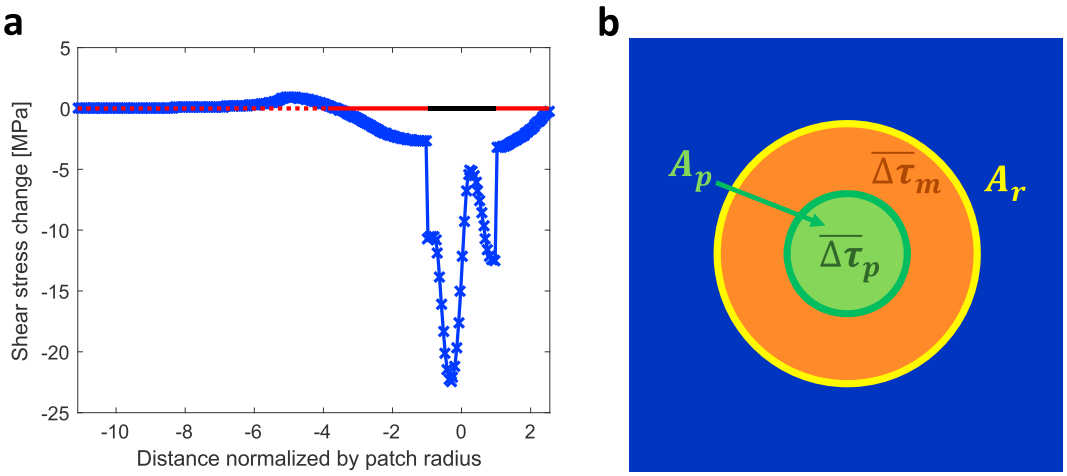

Figure 11. Shear stress changes that are used to derive the simplified stress drop calculation. (a) Horizontal profile of the shear stress change for an intershock from case B (featured in Figure 10a) through the middle of the ruptured patch, shown as a blue line. The qualities of the horizontal line drawn at $y = 0$ indicate whether or not the points for the given part of the profile ruptured in the intershock: dotted red for the unruptured region, solid red for the ruptured area outside of the patch, and solid black for the ruptured area within the patch. (b) Diagram of the quantities required for calculating the simplified average stress drop $\bar{\Delta\tau}_a^{SD}$, including the average shear stress change on the patch $\bar{\Delta\tau}_p$ and off the patch $\bar{\Delta\tau}_m$, the area of the patch A_p, and the total ruptured area A_r. For the featured event, $\bar{\Delta\tau}_p = -10.06$ MPa, $\bar{\Delta\tau}_m = -0.76$ MPa, $D_r/D_p = 3.27$, $\bar{\Delta\tau}_a^{SD} = 2.42$ MPa, and the average moment-based stress drop $\bar{\Delta\tau}^{SD}$ is 2.33 MPa.

3.4. Extended Rupture Area

One might expect that the rupture area of an intershock would be similar to the area of the patch. Instead, we observe that the intershocks can rupture far into the surrounding area (e.g., Figures 1 and 10a), with the rupture extent D_r (equal to twice the effective rupture radius r) depending on the properties of the patch and surrounding area (Figure 12). With the value of the background normal stress σ_m kept constant for this set of simulations, the relative rupture extent D_r/D_p increased approximately linearly with respect to the patch normal stress σ_p (Figure 12, discussed further in section 3.6). This behavior also has important subdependencies. For example, models with no L variation (triangles) or higher instability ratios (blue) have a larger relative rupture extent. Still, the overarching trend is what significantly contributes to moderating the stress drops: The higher the normal stress is on the patch, the relatively further the intershock rupture extends into the surrounding region. This surrounding region enters the average stress computation yet experiences much lower stress changes that range from mild shear stress decreases (positive stress drops) to stress increases (negative stress drops; Figure 10), thus helping to keep the (average) stress drops $\bar{\Delta\tau}^{SD}$ down (equation (6)).

In addition to the dependence on the elevated patch normal stress, the rupture extent should be determined by the response of the surrounding region to the stress change from the expanding seismic event. The (mostly) stress decrease over the rupture area (Figure 10a) is balanced by a stress increase over the rest of the fault, decaying away from the edge of the event (e.g., Kaneko et al., 2010). One can potentially determine D_r/D_p by considering the stress change "balance" over the fault; however, the stress change profiles differ from one case to another beyond the qualitative features discussed here (Figure 11) and hence cannot be readily represented analytically.

3.5. Aseismic Stress Release

In addition to rupturing into the surrounding region, another contributing factor to the reasonable intershock stress drops is aseismic shear stress release. Patches close to their own nucleation size can relieve a significant amount of their shear stress through aseismic slip, closely before the start of the seismic event (e.g., Figure 6, row D). This aseismic release is not included in the (seismic) stress drop $\bar{\Delta\tau}^{SD}$ calculation. The associated aseismic slip occurs due to the intershock nucleation process and can be quite significant. It was previously observed in models of velocity-weakening patches within a velocity-strengthening surrounding (e.g., Chen & Lapusta, 2009; Lui & Lapusta, 2016).

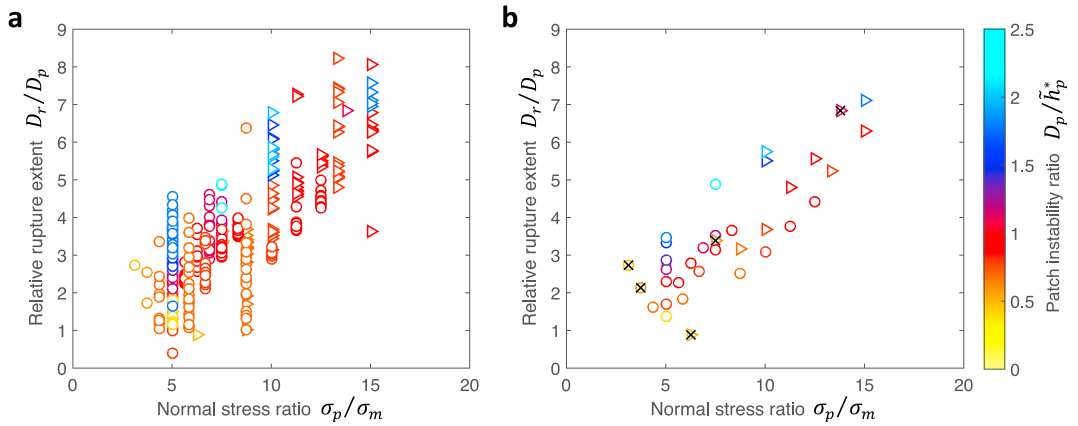

Figure 12. Effect of the patch normal stress on the rupture extent. (a) Relative rupture extent values (effective diameter of ruptured area D_r normalized by the patch diameter D_p) corresponding to each data point in Figure 9, with the same identity scheme. A linear best fit line through the origin has slope γ of approximately 0.41. (b) Median values for each simulation in (a), following the same identity scheme. Median markers for simulations with three or fewer intershocks are indicated by a black "x." The relative rupture extent is approximately linearly dependent on the normal stress ratio σ_p/σ_m on the patch, although it is also affected by the instability ratio $D_p/\tilde{h}_p^*$ (outline color) and characteristic slip ratio L_p/L_m (marker shape). The overall trend results in moderate stress drops $\Delta\bar{\tau}^{SD}$, even for highly compressed patches.

To further investigate this phenomenon, we define the average aseismic stress change to be the shear stress at the start of the seismic event minus the shear stress when the average shear stress is the largest (before the event), averaged over the patch. Analogously, we define the average seismic stress change $\Delta\bar{\tau}_p$ as the shear stress on the patch at the end of the seismic event minus that at the start of the seismic event, averaged over the patch (Figure 11b). The average total stress change is then the sum of the average seismic and aseismic change for a given event. Whenever we report on values for the average seismic, aseismic, or total stress change, we only include intershocks that involve the entire patch to ensure that the average seismic and aseismic stress changes are computed over the same patch area. While most of the simulated intershocks have more average seismic stress change than aseismic, some events have similar values of average seismic and aseismic or even more average aseismic than seismic stress change (Figures 13 –16).

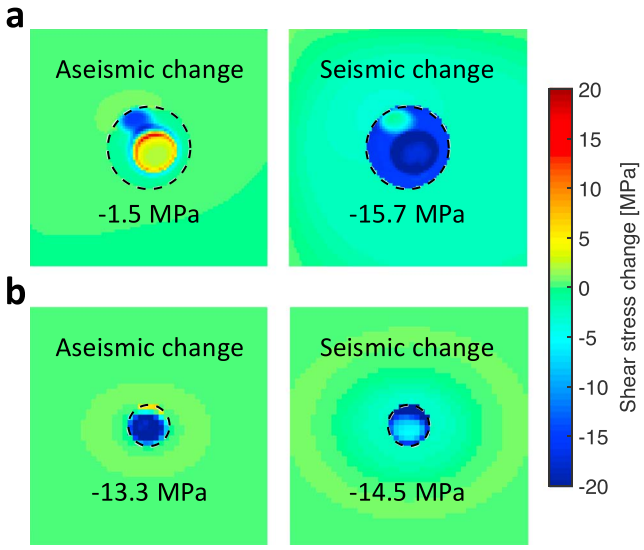

Figure 13. Average aseismic and seismic stress change on the patches, which are outlined with a black dashed line. (a) Spatial distribution of aseismic and seismic stress change for event d.2 in Figure 7 (case C), labeled with values of the average aseismic and seismic stress change averaged over the patch. (b) Same for event a.3 in Figure 7 (case A).

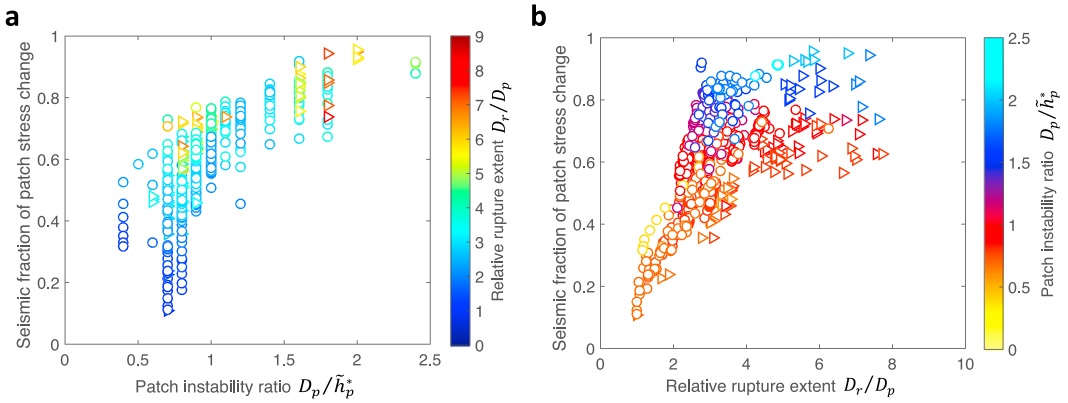

Figure 14. Seismic fraction of average shear stress change on the patch, that is, the ratio of the average seismic stress change to the total one. As the patch instability ratio $D_p/\tilde{h}_p^*$ increases, the total average shear stress change transitions from being mostly aseismic to mostly seismic. (a) The dependence of the average seismic stress change fraction on the patch instability ratio. Unlike Figures 3, 9, and 12, the symbol color indicates relative rupture extent D_r/D_p. Since intershocks within the same simulation can produce different rupture extents, intershocks from the same simulation are no longer represented by the same color. (b) Seismic average stress change fraction versus relative rupture extent, colored by the patch instability ratio. The set of models as well as the identity scheme in this figure is the same as in Figure 9.

It is reasonable to expect that the proportion of average stress change that is aseismic depends on the instability ratio (with one end-member case being a patch that is too small to ever produce seismic events such that all of its stress change is aseismic; e.g., Chen & Lapusta, 2009). Our results show that the fraction of stress relieved seismically is indeed dependent on patch instability ratio $D_p/\tilde{h}_p^*$, with the seismic fraction increasing, overall, with increasing patch instability ratio (Figure 14a), as expected.

For relative rupture extents D_r/D_p around 3.0 and above, widening stripes of constant seismic fraction (Figure 14b) for similar patch instability ratio $D_p/\tilde{h}_p^*$ (outline color), regardless of characteristic slip distance ratio L_p/L_m (shape), imply that the seismic fraction is mostly determined by $D_p/\tilde{h}_p^*$ for high enough $D_p/\tilde{h}_p^*$. We interpret this to reflect the stronger sensitivity of intershocks to the surrounding conditions, that is, slip

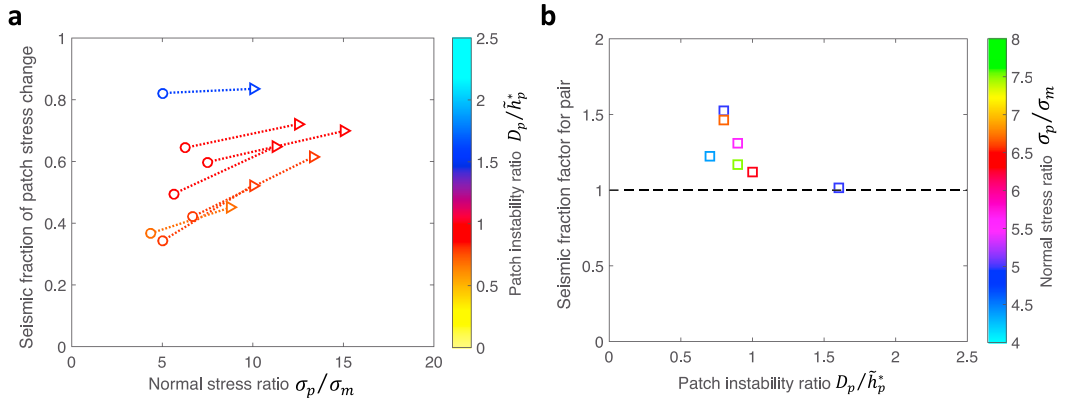

Figure 15. Effect of simultaneously doubling σ_p and L_p on the seismic fraction of average shear stress change on the patch. (a) Median seismic average stress change fractions for pairs of simulations (connected by a dotted line) within the main set that have the same patch diameter D_p and patch instability ratio $D_p/\tilde{h}_p^*$, but for which the same patch nucleation size $\tilde{h}_p^*$ (equation (4)) is achieved by a different combination of patch normal stress σ_p and patch characteristic slip distance L_p. Specifically, reviewing these pairs from left to right, the σ_p and L_p are simultaneously doubled to maintain the $\tilde{h}_p^*$. (b) Seismic fraction factor, that is, the median seismic average stress change fraction of the paired simulation with the higher σ_p and L_p (triangles in (a)) over the median seismic average stress release fraction of the corresponding paired simulation (circles in (a)), versus patch instability ratio. The outline of these square markers is colored by the normal stress ratio of the paired simulation with the lower σ_p and L_p (circles in (a)). All values of the seismic fraction factor are greater than 1, which means that simultaneously doubling σ_p and L_p, for the same D_p and $D_p/\tilde{h}_p^*$, results in intershocks with consistently higher seismic fraction of the total average stress change.

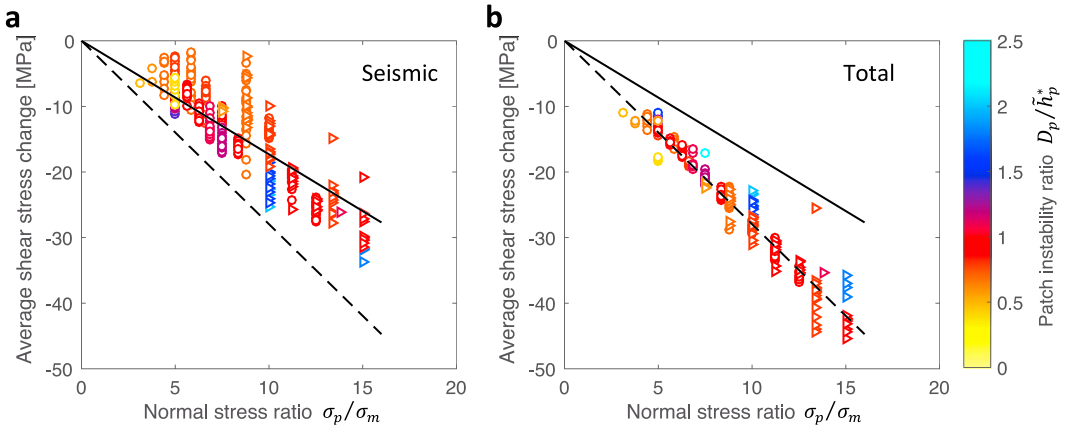

Figure 16. Dependence of the seismic and total average shear stress change (on the patch) of the intershocks on the normal stress ratio for the main set of simulations. The simulation data and identifying marker features correspond to Figure 9. (a) Seismic average shear stress change plotted against the normal stress ratio σ_p/σ_m. The solid black line shows the best linear fit passing through the origin, $\bar{\Delta\tau}_p = -0.17\sigma_p$ (equation (8)). (b) Total average shear stress change versus normal stress ratio. The values for each intershock collapse along the black dashed trendline that passes through the origin, $\bar{\Delta\tau}_{\text{total}} = -0.28\sigma_p$.

history, when initiating on patches that are less prone to instability. This influence creates more variability in the dynamics of the events and thereby a wider range of the resulting seismic fractions for patches with lower instability ratio and a tighter range for patches with higher instability ratio.

The dependence of average aseismic versus seismic stress change on the instability ratio is additionally influenced by the choice of properties assigned to the patch. Models with patches that have the same size D_p and instability ratio $D_p/\tilde{h}_p^*$, but for which the same nucleation size $\tilde{h}_p^*$ is achieved by doubling both σ_p and L_p, produce intershocks with a larger fraction of seismic stress change (Figure 15a). The factor by which the typical seismic fraction of average stress change goes up for models with doubled σ_p and L_p to maintain the same $\tilde{h}_p^*$ decreases overall for increasing $D_p/\tilde{h}_p^*$ (Figure 15b), again indicating that the seismic fraction is mostly determined by $D_p/\tilde{h}_p^*$ for high enough $D_p/\tilde{h}_p^*$. For cases where the instability ratio $D_p/\tilde{h}_p^*$ is low enough, the increase in seismic fraction with increasing patch normal stress σ_p can even flip whether the seismic or aseismic stress release is dominant.

Both the average seismic stress change $\bar{\Delta\tau}_p$ (Figure 16a) and total stress change (Figure 16b) on the patch for the simulated intershocks increase in magnitude with the increasing normal stress σ_p on the patch (recalling that σ_m is held constant). This is in line with the physical intuition that the shear stress changes should be proportional to the normal stress on frictional interfaces. As such, this intuition indeed applies to the patch, but not to the entire seismic event, which includes both the patch and the surrounding ruptured area, as discussed in section 3.4.

Within the overall trend of the increasing magnitude of patch-averaged shear stress change with the increasing normal stress, there is a secondary dependence on patch instability ratio $D_p/\tilde{h}_p^*$. The patches with the highest instability ratios in our set (blue) tend to have more seismic and less total average stress change on the patch than the rest of the models (Figure 16), which would result in steeper and shallower slopes for the seismic and total stress change, respectively. This is because patches with higher instability ratios have their nucleation processes confined to a smaller fraction of the patch, and more of the patch experiences purely seismic stress change. Interestingly, despite resulting in more forceful ruptures on the patch, the total average stress change on the patch tends to be smaller for larger instability ratios, suggesting that the associated smaller nucleation sizes lead to less loaded patches before the rupture initiates (Figure 16b). The slope of the overall trend with respect to the normal stress σ_p is 0.17 and 0.28 for the seismic and total stress release, respectively (Figure 16). Those values are quite similar to the expected slope of 0.20 for the stress drops $\bar{\Delta\tau}^{\text{SD}}$ based on the simulated mainshocks from a homogeneous model (Figure 9, black dotted line) and are related to the selection of the rate-and-state parameters a and b.

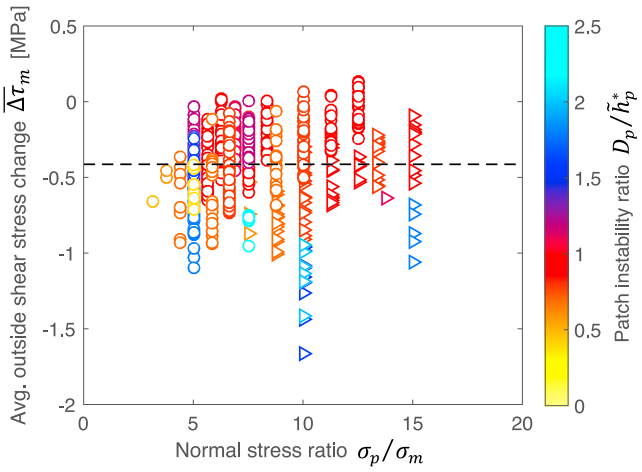

Figure 17. Average shear stress change within the ruptured area outside of the patch $\bar{\Delta\tau}_m$ for intershocks in the main set. The black dashed line shows the mean value of approximately −0.4 MPa. Through dividing this value by the constant background normal stress σ_m of 10 MPa for this set, the coefficient η_m from equation (8) is approximately 0.04.

3.6. Simplified Stress Drop Calculation

Profiles of the change in shear stress through the middle of the ruptured patch illustrate how the stress change varies spatially within the ruptured area (Figure 11a). While the profiles show that the stress change distribution is complicated, it is clear that the average change of stress on the patch $\bar{\Delta\tau}_p$ and off the patch $\bar{\Delta\tau}_m$ (Figure 11b) significantly differ, with the decrease in stress on the patch typically being much larger than the decrease outside. This heterogeneous distribution of the stress change results in the reported moderate stress drops $\bar{\Delta\tau}^{\mathrm{SD}}$.

To gain further insight into the near-constant trend in stress drops $\bar{\Delta\tau}^{\mathrm{SD}}$ with respect to the patch normal stress (Figure 9), we derive a simplified calculation for estimating the stress drop based on parameters from our simulation input and findings of sections 3.4 and 3.5. Using a simple weighted average, we represent the area-based average stress drop $\bar{\Delta\tau}_a^{\mathrm{SD}}$ by the combination of the shear stress changes on the patch and outside of the patch, within the ruptured area:

$$\bar{\Delta\tau}_a^{\mathrm{SD}} = -\left(\bar{\Delta\tau}_p A_p + \bar{\Delta\tau}_m \left(A_r - A_p\right)\right)/A_r. \tag{7}$$

Assuming that both the patch and ruptured area are circular, one gets $A_p = \pi D_p^2/4$ and $A_r = \pi D_r^2/4$. Based on our simulation results, we assume the following approximate relationships:

$$\frac{D_r}{D_p} = \gamma\frac{\sigma_p}{\sigma_m}, \quad \bar{\Delta\tau}_p = -\eta_p\sigma_p, \text{ and } \bar{\Delta\tau}_m = -\eta_m\sigma_m, \tag{8}$$

where γ, η_p, and η_m are taken as constants but may depend on the model parameters. Inserting these relationships into equation (7) results in

$$\bar{\Delta\tau}_a^{\mathrm{SD}} = \left(\frac{\eta_p}{\gamma^2}\frac{\sigma_m}{\sigma_p} + \eta_m - \frac{\eta_m}{\gamma^2}\frac{\sigma_m^2}{\sigma_p^2}\right)\sigma_m, \tag{9}$$

revealing that the relation between the stress drops of intershocks and the normal stress ratio σ_p/σ_m in this approximation is dependent on the background normal stress σ_m and three constants that are likely dependent on the rate-and-state parameters, especially a and b. In the case of no patch of higher normal stress, one gets $\sigma_p = \sigma_m$, $A_p = A_r$, and $\eta_p = \eta_m$, resulting in $\bar{\Delta\tau}_a^{\mathrm{SD}} = \eta_m\sigma_m$ from equation (9), which is expected.

For many intershocks in our models, the rupture dimension D_r is much larger than the patch diameter D_p, which leads us to another insightful simplification. In this case, $D_r \gg D_p$, so $A_r \gg A_p$, resulting in $A_r - A_p \approx A_r$. Applying this reduction to equation (7) and inserting the relationships from equation (8) gives

$$\bar{\Delta\tau}_a^{\mathrm{SD}} = \left(\frac{\eta_p}{\gamma^2}\frac{\sigma_m}{\sigma_p} + \eta_m\right)\sigma_m. \tag{10}$$

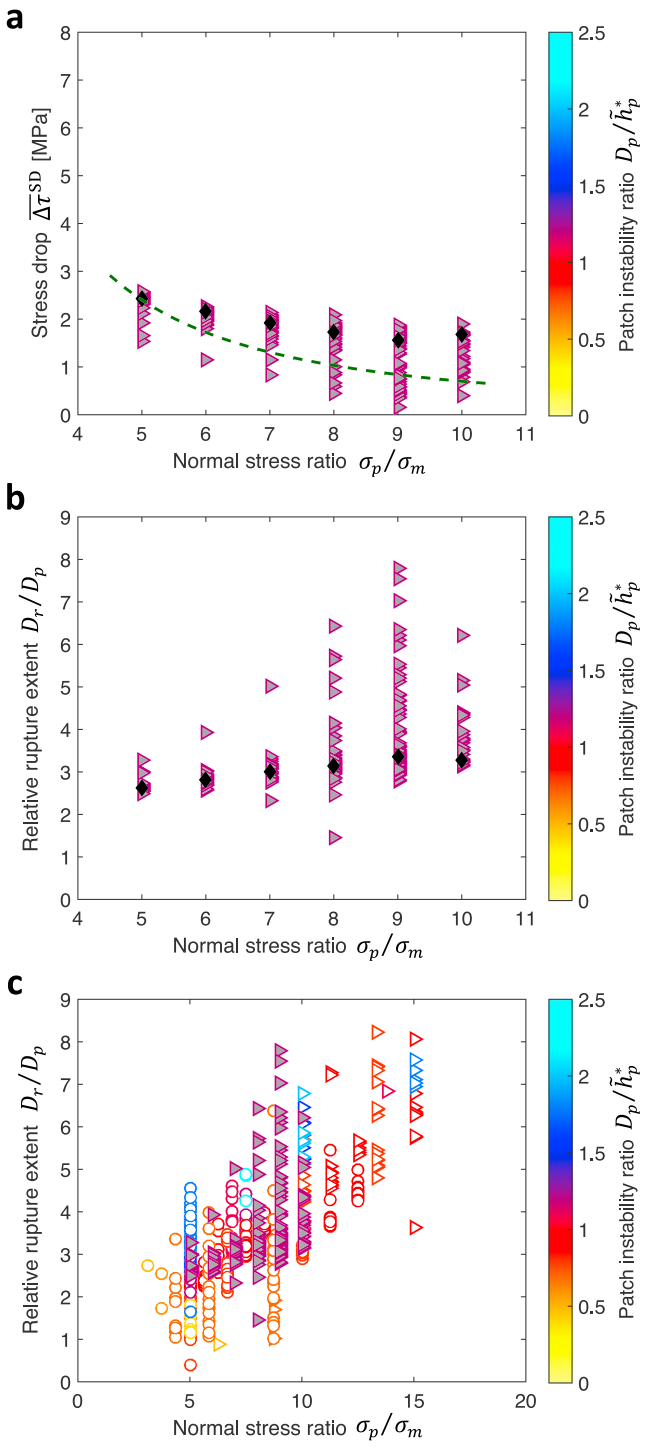

Figure 18. Results for the Variable Background Normal Stress (VBNS) set of simulations. (a) Stress drops $\bar{\Delta\tau}^{SD}$ of the intershocks. The green dashed line shows the trend from the simplified stress drop calculation ($\bar{\Delta\tau}_a^{SD}$, equation (10)). Black diamonds indicate the median values for each simulation. (b) Effect of patch normal stress ratio σ_p/σ_m on relative rupture extent D_r/D_p for the VBNS set, with medians. (c) The relative rupture extents for the main set from Figure 12a with those from the VBNS set in (b) overlaid. For (b) and (c), note that the two VBNS simulations with the highest normal stress ratio ($\sigma_p/\sigma_m = 9, 10$) each have one data point that is outside of the y axis limits of these plots ($D_r/D_p = 12.8, 14.2$, respectively). The identity scheme for the data markers is the same as in Figure 3.

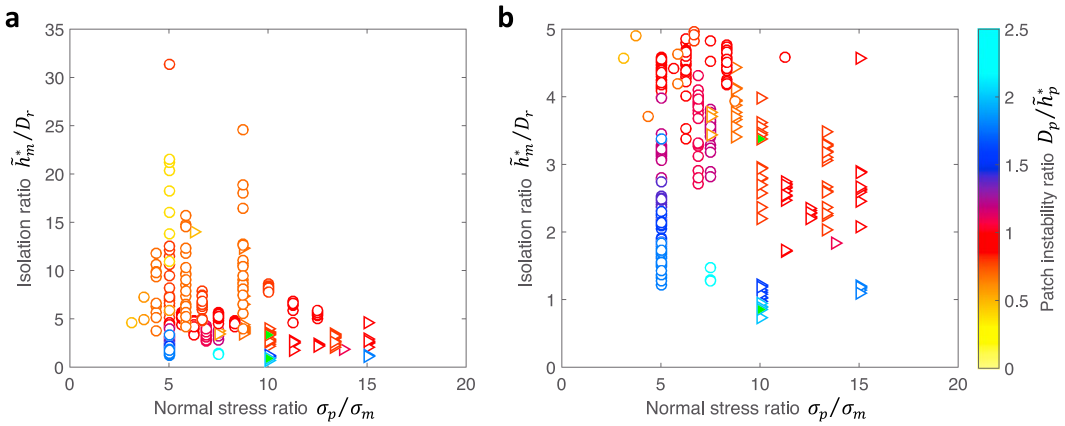

Figure 19. Isolation ratio $\tilde{h}_m^*/D_r$ for the main set of models. The data and marker identity scheme correspond to Figure 9. The two intershocks indicated by green-filled markers are analyzed further in Figure 20. (a) Values for all intershocks. The highest point, $\tilde{h}_m^*/D_r = 31.33$, is for an intershock that only partially ruptured the patch, that is, $D_r/D_p < 1$, as seen in Figure 12a. (b) Same data as in (a) but zoomed into the isolation ratios between 0 and 5.

For the main set of models in our study, the constants in equation (10) can be calculated from linear fits for our simulation results: $\gamma \approx 0.41$ from Figure 12a, $\eta_p \approx 0.17$ from Figure 16a, and $\eta_m \approx 0.04$ from finding the average $\bar{\Delta\tau}_m$ (recalling that σ_m was held constant; Figure 17). Using these constants results in $\bar{\Delta\tau}_a^{SD} = \left(\sigma_m/\sigma_p + 0.04\right)\sigma_m$, because $\eta_p/\gamma^2 \approx 1$ for this particular case. While the first term in this equation dominates for all of the models in this study, the second term would begin to dominate for $\sigma_p/\sigma_m > 25$.

The trend predicted by this equation (Figure 9, green dashed line) explains the main features of dependence on σ_p/σ_m, including the relatively low values of $\bar{\Delta\tau}^{SD}$ and the slight decrease of $\bar{\Delta\tau}^{SD}$ with σ_p/σ_m. It is important to note that the simplified stress drop calculation created here uses area-based averaging ($\bar{\Delta\tau}_a^{SD}$), whereas the stress drops computed in the simulations are moment-based ($\bar{\Delta\tau}^{SD}$, equation (6)), but the values of the two types of average stress drops are typically similar, with the area-based values usually smaller than the moment-based (Noda et al., 2013).

Given that the background normal stress σ_m for models in the main set is held constant, we developed the VBNS set (section 2.3 and Table 3) to test the dependence of stress drops on σ_m, illuminated by the simplified stress drop formulation $\bar{\Delta\tau}_a^{SD}$ (equation (9)). The stress drops $\bar{\Delta\tau}^{SD}$ for the VBNS set are well-approximated by the simplified estimate $\bar{\Delta\tau}_a^{SD}$ (Figure 18a) with the coefficients derived from the main set (equation (10)). Furthermore, we find that the relative rupture extents D_r/D_p for the intershocks from the VBNS set overlap well with the those from the main set (Figure 18c), although the coefficient γ derived for the VBNS set alone (Figure 18b) would be lower than that derived for the main set overall (which could simply be from the focus on a single patch instability ratio $D_p/\tilde{h}_p^*$).

The stress drops from the simplified estimate $\bar{\Delta\tau}_a^{SD}$ for both the main set and VBNS set fit well overall but tend to decrease with the normal stress ratio σ_p/σ_m faster than the stress drops calculated for these events via the standard formulation $\bar{\Delta\tau}^{SD}$ (Figures 9 and 18a). The assumption, made for simplicity, that the coefficients γ, η_p, and η_m are constant contributes to this difference. As discussed in the previous sections, there is some evidence that these constants are additionally dependent on other parameters, for example, on the patch instability ratio $D_p/\tilde{h}_p^*$, with higher $D_p/\tilde{h}_p^*$, and hence, in general, higher σ_p/σ_m, corresponding to higher constants (e.g., blue symbols in Figures 12a, 16a, and 17). Still, our simplified stress drop calculation is successful in approximately matching the trend in stress drops $\bar{\Delta\tau}^{SD}$, especially given its simplicity.

3.7. Rupture Extent of Intershocks Versus the Larger-Scale Nucleation Size

The intershocks presented in this work are, by definition, patch-initiated seismic events that are isolated, that is, do not turn into mainshocks. Let us further consider the required separation of length scales, where a rearrangement of equation (5) reveals

$$\frac{h_m^*}{h_p^*} = \frac{h_m^*}{D_r}\frac{D_r}{D_p}\frac{D_p}{h_p^*}. \tag{11}$$

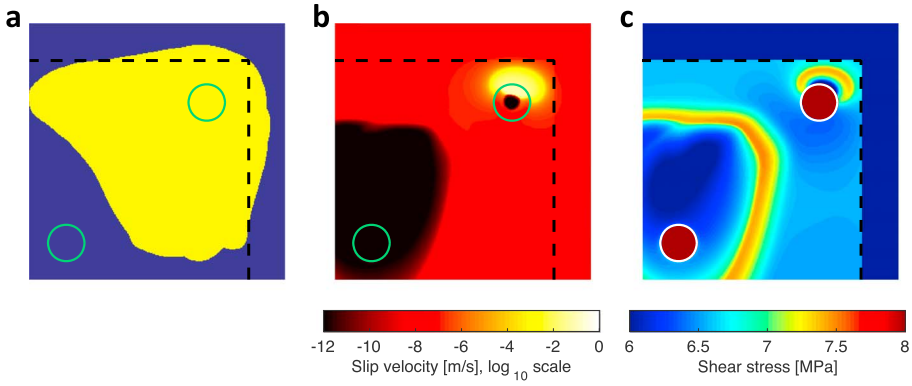

Figure 20. Intershock rupture extent and initiation conditions for one case of low isolation ratio $\tilde{h}_m^*/D_r$. (a) The ruptured area of the event (yellow). (b) Snapshot of the slip velocity on a log scale. (c) The shear stress at the start of the intershock. The fault model has the same properties as case A (σ_p/σ_m, L_p/L_m, and $\tilde{h}_m^*/\tilde{h}_p^*$), except the patch diameter is 2.5 times larger and, consequently, the patch instability ratio $D_p/\tilde{h}_p^*$ is 2.0 instead of 0.8 and has $\tilde{h}_m^*/D_r = 0.85$. The color scale for the shear stress snapshot is cropped to highlight the falloff in stress from the creeping section to the locked middle portion of the fault. In all subplots, the boundary between the velocity-weakening and velocity-strengthening region is indicated by a black dashed line, and the circular patch is outlined for clarity.

For the main set of simulations, the instability ratio $D_p/\tilde{h}_p^*$ is between 0.4 and 2.4 (section 2.3), and the relative rupture extent D_r/D_p is between approximately 1 and 9 (section 3.4). As previously mentioned (section 2.2), besides the patch instability ratio $D_p/\tilde{h}_p^*$ and the spacing between the patches, the occurrence of intershocks is dependent on the ratio of the mainshock nucleation size to the intershock rupture dimension h_m^*/D_r, which we call the isolation ratio. For a seismic event initiating on a patch to avoid immediately triggering a mainshock, h_m^* must be sufficiently larger than D_r.

The main set of simulations (Table 2) provides insight into the values of $\tilde{h}_m^*/D_r$ that result in intershocks, ranging from $\tilde{h}_m^*/D_r \approx 31$ for the smallest events to $\tilde{h}_m^*/D_r \approx 1$ for the largest events (Figure 19a), with most values of $\tilde{h}_m^*/D_r$ between ≈2 and 10. As expected, the lowest isolation ratios occur for the models with the highest patch instability ratios $D_p/\tilde{h}_p^*$ (also the largest patches), as patches in these models have the most potential for initiating healthy ruptures. Interestingly, many of the corresponding isolation ratios are close to 1 and some are even slightly below 1 (Figure 19b), meaning that ruptures with D_r greater than but close to $\tilde{h}_m^*$ can still avoid growing into a mainshock.

The unexpected observation of $\tilde{h}_m^*/D_r \approx 1$ still allowing for intershocks, that is, patch-initiated events not growing large enough to be considered mainshocks, in certain cases merits an investigation. We find that this occurs when the intershock is initiated early in the nucleation process, before a sufficiently large portion of the velocity-weakening region is loaded enough to be ready for a mainshock, making the stress distribution at the start of the intershock unfavorable for rupture growth; then seismic events with rupture extent D_r close to $\tilde{h}_m^*$ can still arrest. Figure 20 provides a map of the ruptured area and both the slip rate V and shear stress τ at the start of the seismic event for an example of an intershock with $\tilde{h}_m^*/D_r < 1$. In this example, it is apparent that the low shear stress in the locked portion of the fault, due to the previous mainshock, creates unfavorable conditions that stunt the rupture (Figure 20), preventing the event from growing into a mainshock. Thereby, $\tilde{h}_m^*/D_r$ can be about 1 and still allow for intershocks but cannot be much smaller: $\tilde{h}_m^*/D_r = 0.74$ is the smallest that we have seen in our main set. Furthermore, in terms of their timing, the most foreshock-like events would occur in the later stages of the nucleation of the mainshock and therefore require a higher isolation ratio, significantly larger than 1.

We infer that the isolation ratio h_m^*/D_r for producing intershocks that are fully isolated from the upcoming mainshock is most strongly dependent on the following three factors: (1) the instability ratio of the patch D_p/h_p^*, where higher instability ratios generally correspond to more dramatic ruptures that can more strongly perturb the surrounding region, thereby reducing the background nucleation size h_m^*; (2) the instability ratio of the background seismogenic region W_{VW}/h_m^*, which indicates how easy it is to instigate dynamic rupture on a larger scale; and (3) the pre-intershock state of shear stress on the fault, which is a combination of the stress left over from previous events and the loading from the creeping region (e.g., Figure 20). Additional factors that can influence the stress state at the start of the event, and thereby the ratio

h_m^*/D_r through D_r, are the spacing between patches and the interaction between sequential intershocks via postseismic slip, but these two factors are beyond the scope of this study.

Recalling section 2.2 and equation (11), the core of the separation of length scales is the separation between the nucleation size of the intershocks h_p^* and the nucleation size of the mainshocks h_m^*. The separation ratio $\tilde{h}_m^*/\tilde{h}_p^*$ for all of the models in both the main set and VBNS set fall between 6 and 25.

4. Discussion: Linking to Natural Faults

While the spatial scale and parameters in our simulations are inspired by laboratory experiments (McLaskey & Kilgore, 2013; McLaskey et al., 2014), the qualitative features and trends in our results should be relevant to natural faults. In line with the growing perspective that foreshocks are created by the interaction of slow slip with favorable fault patches (Bouchon et al., 2013; Brodsky & Lay, 2014; Dodge et al., 1995; Jones & Molnar, 1979; Kanamori & Stewart, 1978; Kato et al., 2012; McGuire et al., 2005), we have shown that the scenario of asperity-type patches of elevated compression as initiation locations for foreshocks driven by the larger-scale nucleation process is indeed physically plausible. Natural faults in the laboratory and the field likely have much more distributed and varied heterogeneity than that assumed in our models, but only the spots where properties are favorable for producing smaller-scale seismicity are seen via intershocks.

Our results suggest that faults with numerous foreshocks likely have properties corresponding to a relatively large background nucleation size h_m^* in relation to the foreshock rupture size D_r; otherwise, the potential foreshocks would just grow into the main event. The microseismic events interpreted as foreshocks on natural faults typically have moment magnitudes M_w of 2–3, which correspond to the source dimensions around 100–400 m. The larger-scale nucleation size, then, has to be approximately 1–8 km for cases with foreshock sequences.

In fact, the relatively recently discovered slow slip transients in subduction zones (Dragert et al., 2001; Peng & Gomberg, 2010; Schwartz & Rokosky, 2007) potentially provide evidence for at least occasional fault conditions in which the background nucleation size is quite large. In the slow slip transients, fault slip rates spontaneously accelerate to values 2–3 orders of magnitude above the plate rate but remain 5–6 orders of magnitude below the seismic slip rates. These quasi-static events can be modeled essentially as a protracted large-scale nucleation process that migrates along the fault (Liu & Rice, 2007; Segall et al., 2010). The transients can travel hundreds of kilometers along the fault but occupy a width of the order of 10 km at the bottom of the seismogenic zone, suggesting the nucleation size estimate of that order. Some of these slow slip events are accompanied by a seismic signal called tremor, which is interpreted as a myriad of barely seismic events (called low-frequency earthquakes) triggered by the slow slip and occurring so frequently that their signals overlap (e.g., Peng & Gomberg, 2010; Shelly et al., 2007, 2006). Earthquake nucleation with foreshock sequences, then, may be a somewhat smaller-scale version of these aseismic transients that occurs in the presence of fault heterogeneity suitable for producing more traditional microseismicity.

In the context of rate-and-state friction with laboratory-based properties and nucleation estimates given by equation (3), such large nucleation sizes require sufficiently low effective normal stresses, of the order of 1 MPa or even less, depending on the rate-and-state properties. For example, given the typical values for rate-and-state properties based on laboratory findings and also used in models that reproduce microseismic observations (e.g., Chen & Lapusta, 2009, and references therein) of $a = 0.01$, $b = 0.014$, and $L = 100\,\mu$m, the effective normal stress needs to be approximately 5–0.5 MPa for mainshock nucleation sizes of 1–8 km.

Another factor that would allow for large background nucleation sizes on natural faults is inelastic shear dilatancy and the associated pore pressure effects (Liu & Rubin, 2010; Marone et al., 1990; Segall et al., 2010; Segall & Rice, 1995), which can make the nucleation size arbitrarily large or infinite, even on steady-state velocity-weakening faults. For a laboratory-based dilatancy formulation and properties (Segall et al., 2010; Segall & Rice, 1995), the reference effective normal stress still has to be relatively low to allow for sufficiently large nucleation sizes, but not as low as for the standard rate-and-state friction formulation alone.

While our lab-motivated models thus far have not involved fluids, and therefore effective normal stress and normal stress have been synonymous, natural faults are often permeated with fluids, with the effective normal stress being the elastodynamic normal stress minus the pore pressure. To achieve the required low effective normal stresses at seismogenic depths, the faults must have the pore fluid pressure much beyond

the hydrostatic level. Such high pore pressure conditions can be achieved locally around faults, as the faults may serve as conduits to fluids generated by dehydration reactions at depth (e.g., Liu & Rice, 2007; Rice, 1992), because of the lower fault-parallel permeability due to persistent slip and near-fault damage. In addition, the state of highly elevated pore pressure may be transient, since the episodes of pore fluids entering the fault at depth may be episodic.

Factors unrelated to elevated pore fluid pressure and its variations due to dilatancy can cause large background nucleation sizes as well, including near-velocity-neutral (i.e., near-zero) values of the rate-and-state parameter $a - b$ and values of characteristic slip L much larger than the ones found in the laboratory, as clear from equation (3). A combination of these factors and pore pressure effects is also a possibility.

Although we did not thoroughly explore it in this study, the sufficiently fast creeping rate may be an important factor for producing intershocks on highly compressed patches. We have seen that accelerated creep can encourage patches to rupture sooner (Figure 8) and that patches may never produce intershocks if the interseismic loading is not enough to overcome their high compression (filled purple triangle in Figure 3). Given that all of the patches in our models have significantly higher compression than the background, it is possible that observable asperity-type seismic events on natural faults only occur for the highest creeping rates, such as the ones during earthquake nucleation.

Our results also suggest that the foreshock sequences on natural faults would be promoted by low instability ratios for asperity-type patches. Low patch instability ratios D_p/h_p^* promote separated seismic events during the nucleation of a mainshock that do not grow into the mainshock, because lower instability ratios generally correspond to a smaller rupture extent D_r and thereby a higher isolation ratio h_m^*/D_r. Furthermore, high patch instability ratios D_p/h_p^* would require high levels of heterogeneity in the fault properties—to achieve the required small nucleation size h_p^*—that may be less likely.

Overall, observable foreshocks likely occur in the "sweet spot" with respect to fault heterogeneity: If the heterogeneity is too mild, so that the instability ratios on patches are significantly below 1, then there is no potential for microseismicity; but if the heterogeneity is too strong, then the patch-initiated events would either grow into the mainshock immediately or the patches may not receive enough loading to rupture during the aseismic nucleation, failing during the subsequent larger-scale dynamic event instead.

As discussed in section 1, our consideration of the patches of elevated normal stress is motivated by the suggestion from the laboratory experiments (McLaskey & Kilgore, 2013; McLaskey et al., 2014) that foreshock-like events occur in the same persistent locations on the experimental interface, likely corresponding to fault nonplanarities or bumps, and the inference that natural faults are nonplanar (Brodsky et al., 2011; Candela et al., 2009; Renard et al., 2006; Sagy et al., 2007). In this study, we account for the most relevant effect of the nonplanarity, which is the potential for significantly increased normal stress locally. On a realistically nonplanar interface, there would be a complex distribution of the normal stress evolving with slip (e.g., Dunham et al., 2011). The patches considered in this study would correspond to areas of the fault where the normal stress is sufficiently elevated on average. In order to produce events with source dimensions of 100–400 m as discussed above, the areas would be much larger than fault slip over tens and even hundreds of years and hence would be persistent. Simulations of earthquake sequences and slow slip with the differences in the nucleation sizes considered in this study and inertial effects on realistically nonplanar interfaces are currently not tractable but would be important to conduct once the numerical capabilities and computational resources further improve.

5. Conclusions

The rate-and-state fault models with patches of elevated normal stress can indeed produce smaller-scale seismicity—intershocks—driven by the slow slip of the mainshock nucleation, for reasonable parameters. For intershocks to occur, that is, for smaller-scale seismicity to remain isolated from the mainshocks as distinct events, we find that a significant separation in nucleation length scales is needed. In our models, this is achieved by a significant increase of normal stress on the patch, by up to a factor of 15, and, in some cases, and additional decrease in the characteristic slip distance.

Contrary to the expectation that much higher normal stress on the patch would produce unreasonably high stress drops, our intershock sources produce reasonable stress drops that are nearly constant over the explored range of the patch normal stress. Moreover, they match the typical stress drops observed in the

laboratory and the field. This potentially surprising but crucial behavior is achieved by two main mechanisms: (1) ruptures extending into the surrounding region and (2) aseismic stress release just prior to the start of the seismic event.

Our setup of velocity-weakening patches within a larger velocity-weakening region allows seismic events originating on patches of higher compression to extend significantly outside of the patch. The rupture extent clearly depends on the instability ratio of the patch. In addition, our simulation results show that the rupture dimension relative to the patch size increases with increasing patch normal stress. This extended rupture dimension controls the stress drop, particularly for patches with highly elevated normal stress.

Most significantly for patches that are similar in dimension to their nucleation size, aseismic stress release also contributes to the reasonable stress drops. Due to the slow pace of this stress release, these patches are able to alleviate some of the accumulated shear stress in a way that is not included in the seismic stress drop calculation.

The appropriate separation in length scales for producing separated smaller-scale events, that is, intershocks, depends on various interconnected factors, such as nucleation sizes and instability ratios of both the patches and surrounding seismogenic region, intershock rupture extent, mainshock nucleation size relative to the intershock rupture extent, and the shear stress distribution left over from the history of past events. Nonetheless, the two quantities that we have found to be the most relevant (though incomplete) in controlling the occurrence of intershocks are the patch instability ratio D_p/h_p^* and the isolation ratio h_m^*/D_r. The former influences the potential for seismic rupture and the capacity for a healthy dynamic rupture, and the latter influences the potential for smaller-scale dynamic events to end before they immediately trigger and thereby blend into the mainshock. Additionally, although we did not explicitly explore patch spacing in this study, it is reasonable to assume that patch spacing would play a role in the occurrence of intershocks, with closely spaced patches potentially turning into compound events and far-spaced patches being effectively ignored by the mainshock nucleation.

The success of our model in producing two separate scales of seismic events within the same seismogenic zone, with the smaller-scale events having reasonable stress drops despite the heterogeneous properties, provides important insight into the conditions suitable for the occurrence of intershocks on both laboratory and natural faults. In particular, our results suggest that faults with observable intershocks likely have a relatively large mainshock nucleation size as well as localized areas with much smaller nucleation size and properties corresponding to a relatively low instability ratio.

Note that the focus of this study is on the detailed dynamic behavior of single smaller-scale seismic events driven by larger-scale nucleation creep. Our model is too simple to consider realistic sequences or statistical properties of the resulting microseismicity and hence to determine whether those outcomes would be consistent with foreshock observations. However, the relative geometric simplicity of the model has allowed us to produce and study well-resolved, elastodynamically consistent models of the microseismic events. A potential next step in considering the more general problem of foreshocks would be to assume realistically heterogeneous fault properties over a much larger fault segment and replace the (computationally intractable) detailed simulations of each microseismic event in such a model with sources precomputed based on the simulations in this study, to consider their collective properties, interaction, and statistics.

Acknowledgments
This study was supported by the National Science Foundation (grants EAR 1520907 and 1724686) and the Southern California Earthquake Center (SCEC), contribution 8972. SCEC is funded by NSF Cooperative Agreement EAR-1600087 and USGS Cooperative Agreement G17AC00047. The numerical simulations for this work were run on the supercomputing cluster in the Caltech Division for Geology and Planetary Science. The data supporting the analysis and conclusions are given in figures and tables. We thank Greg McLaskey for insightful discussions about the laboratory experiments, Jean-Philippe Avouac and Tom Heaton for helpful comments to the manuscript, and Junle Jiang for help with the simulation code.

References

Abercrombie, R. E. (1995). Earthquake source scaling relationships from −1 to 5 M_L using seismograms recorded at 2.5-km depth. *Journal of Geophysical Research*, *100*(B12), 24,015–24,036. https://doi.org/10.1029/95JB02397

Abercrombie, R. E., & Mori, J. (1996). Occurrence patterns of foreshocks to large earthquakes in the western United States. *Nature*, *381*(6580), 303–307. https://doi.org/10.1038/381303a0

Bizzarri, A., & Belardinelli, M. E. (2008). Modelling instantaneous dynamic triggering in a 3-D fault system: Application to the 2000 June South Iceland seismic sequence. *Geophysical Journal International*, *173*(3), 906–921. https://doi.org/10.1111/j.1365-246X.2008.03765.x

Bouchon, M., Durand, V., Marsan, D., Karabulut, H., & Schmittbuhl, J. (2013). The long precursory phase of most large interplate earthquakes. *Nature Geoscience*, *6*(4), 299–302. https://doi.org/10.1038/ngeo1770

Bouchon, M., Karabulut, H., Aktar, M., Özalaybey, S., Schmittbuhl, J., & Bouin, M.-P. (2011). Extended nucleation of the 1999 M_w 7.6 Izmit earthquake. *Science*, *331*(6019), 877–880. https://doi.org/10.1126/science.1197341

Bowman, D. D., & King, G. C. (2001). Accelerating seismicity and stress accumulation before large earthquakes. *Geophysical Research Letters*, *28*(21), 4039–4042. https://doi.org/10.1029/2001GL013022

Brodsky, E. E., Gilchrist, J. J., Sagy, A., & Collettini, C. (2011). Faults smooth gradually as a function of slip. *Earth and Planetary Science Letters*, *302*(1–2), 185–193. https://doi.org/10.1016/j.epsl.2010.12.010

Brodsky, E. E., & Lay, T. (2014). Recognizing foreshocks from the 1 April 2014 Chile earthquake. *Science*, *344*(6185), 700–702. https://doi.org/10.1126/science.1255202

Candela, T., Renard, F., Bouchon, M., Brouste, A., Marsan, D., Schmittbuhl, J., & Voisin, C. (2009). Characterization of fault roughness at various scales: Implications of three-dimensional high resolution topography measurements. In Y. Ben-Zion, & C. Sammis (Eds.), *Mechanics, structure and evolution of fault zones* (pp. 1817–1851). Berlin: Springer.

Chen, T., & Lapusta, N. (2009). Scaling of small repeating earthquakes explained by interaction of seismic and aseismic slip in a rate and state fault model. *Journal of Geophysical Research*, *114*, B01311. https://doi.org/10.1029/2008JB005749

Day, S. M., Dalguer, L. A., Lapusta, N., & Liu, Y. (2005). Comparison of finite difference and boundary integral solutions to three-dimensional spontaneous rupture. *Journal of Geophysical Research*, *110*, B12307. https://doi.org/10.1029/2005JB003813

Dieterich, J. H. (1979). Modeling of rock friction: 1. Experimental results and constitutive equations. *Journal of Geophysical Research*, *84*(B5), 2161–2168. https://doi.org/10.1029/JB084iB05p02161

Dieterich, J. H. (1992). Earthquake nucleation on faults with rate-and state-dependent strength. *Tectonophysics*, *211*(1–4), 115–134. https://doi.org/10.1016/0040-1951(92)90055-B

Dieterich, J. H. (2007). Applications of rate-and state-dependent friction to models of fault slip and earthquake occurrence. *Treatise on Geophysics*, *4*, 107–129. https://doi.org/10.1016/B978-044452748-6/00065-1

Dieterich, J. H., & Kilgore, B. (1996). Implications of fault constitutive properties for earthquake prediction. *Proceedings of the National Academy of Sciences*, *93*(9), 3787–3794. https://doi.org/10.1073/pnas.93.9.3787

Dodge, D. A., Beroza, G. C., & Ellsworth, W. L. (1995). Foreshock sequence of the 1992 Landers, California, earthquake and its implications for earthquake nucleation. *Journal of Geophysical Research*, *100*(B6), 9865–9880. https://doi.org/10.1029/95JB00871

Dodge, D. A., Beroza, G. C., & Ellsworth, W. (1996). Detailed observations of California foreshock sequences: Implications for the earthquake initiation process. *Journal of Geophysical Research*, *101*(B10), 22,371–22,392. https://doi.org/10.1029/96JB02269

Doser, D. I. (1990). Foreshocks and aftershocks of large ($M \geq 5.5$) earthquakes within the Western Cordillera of the United States. *Bulletin of the Seismological Society of America*, *80*(1), 110–128.

Dragert, H., Wang, K., & James, T. S. (2001). A silent slip event on the deeper Cascadia subduction interface. *Science*, *292*(5521), 1525–1528. https://doi.org/10.1126/science.1060152

Dunham, E. M., Belanger, D., Cong, L., & Kozdon, J. E. (2011). Earthquake ruptures with strongly rate-weakening friction and off-fault plasticity, part 2: Nonplanar faults. *Bulletin of the Seismological Society of Amertica*, *101*(5), 2308–2322. https://doi.org/10.1785/0120100076

Eshelby, J. D. (1957). The determination of the elastic field of an ellipsoidal inclusion, and related problems. In *Proceedings of the Royal Society of London, Series A*, vol. 241, The Royal Society, pp. 376–396. https://doi.org/10.1098/rspa.1957.0133

Heaton, T. H. (1990). Evidence for and implications of self-healing pulses of slip in earthquake rupture. *Physics of the Earth and Planetary Interiors*, *64*(1), 1–20. https://doi.org/10.1016/0031-9201(90)90002-F

Higgins, N., & Lapusta, N. (2017). Exploring models of foreshock sources using rate-and-state friction. In J. M. Floryan (Ed.), *Contributions to the foundations of multidisciplinary research in mechanics* (Vol. 3, pp. 2148–2149). Ottawa: National Research Council Canada.

Jiang, J., & Lapusta, N. (2017). Connecting depth limits of interseismic locking, microseismicity, and large earthquakes in models of long-term fault slip. *Journal of Geophysical Research: Solid Earth*, *122*, 6491–6523. https://doi.org/10.1002/2017JB014030

Jones, L., & Molnar, P. (1976). Frequency of foreshocks. *Nature*, *262*(5570), 677–679. https://doi.org/10.1038/262677a0

Jones, L. M., & Molnar, P. (1979). Some characteristics of foreshocks and their possible relationship to earthquake prediction and premonitory slip on faults. *Journal of Geophysical Research*, *84*(B7), 3596–3608. https://doi.org/10.1029/JB084iB07p03596

Kanamori, H., & Anderson, D. L. (1975). Theoretical basis of some empirical relations in seismology. *Bulletin of the Seismological Society of America*, *65*(5), 1073–1095.

Kanamori, H., & Stewart, G. S. (1978). Seismological aspects of the Guatemala earthquake of February 4, 1976. *Journal of Geophysical Research*, *83*(B7), 3427–3434. https://doi.org/10.1029/JB083iB07p03427

Kaneko, Y., Avouac, J.-P., & Lapusta, N. (2010). Towards inferring earthquake patterns from geodetic observations of interseismic coupling. *Nature Geoscience*, *3*(5), 363–369. https://doi.org/10.1038/ngeo843

Kaneko, Y., & Lapusta, N. (2008). Variability of earthquake nucleation in continuum models of rate-and-state faults and implications for aftershock rates. *Journal of Geophysical Research*, *113*, B12312. https://doi.org/10.1029/2007JB005154

Kaneko, Y., Nielsen, S. B., & Carpenter, B. M. (2016). The onset of laboratory earthquakes explained by nucleating rupture on a rate-and-state fault. *Journal of Geophysical Research: Solid Earth*, *121*, 6071–6091. https://doi.org/10.1002/2016JB013143

Kato, A., Obara, K., Igarashi, T., Tsuruoka, H., Nakagawa, S., & Hirata, N. (2012). Propagation of slow slip leading up to the 2011 M_w9.0 Tohoku-Oki earthquake. *Science*, *335*(6069), 705–708. https://doi.org/10.1126/science.1215141

Lapusta, N., & Liu, Y. (2009). Three-dimensional boundary integral modeling of spontaneous earthquake sequences and aseismic slip. *Journal of Geophysical Research*, *114*, B09303. https://doi.org/10.1029/2008JB005934

Lapusta, N., Rice, J. R., Ben-Zion, Y., Zheng, G., & Journal of Geophysical Research (2000). Elastodynamic analysis for slow tectonic loading with spontaneous rupture episodes on faults with rate-and state-dependent friction, *105*(B10), 23,765–23,789. https://doi.org/10.1029/2000JB900250

Lengliné, O., Elkhoury, J., Daniel, G., Schmittbuhl, J., Toussaint, R., Ampuero, J.-P., & Bouchon, M. (2012). Interplay of seismic and aseismic deformations during earthquake swarms: An experimental approach. *Earth and Planetary Science Letters*, *331*, 215–223. https://doi.org/10.1016/j.epsl.2012.03.022

Liu, Y., & Rice, J. R. (2007). Spontaneous and triggered aseismic deformation transients in a subduction fault model. *Journal of Geophysical Research*, *112*, B09404. https://doi.org/10.1029/2007JB004930

Liu, Y., Rice, J. R., & Larson, K. M. (2007). Seismicity variations associated with aseismic transients in Guerrero, Mexico, 1995–2006. *Earth and Planetary Science Letters*, *262*(3–4), 493–504. https://doi.org/10.1016/j.epsl.2007.08.018

Liu, Y., & Rubin, A. M. (2010). Role of fault gouge dilatancy on aseismic deformation transients. *Geophysical Research Letters*, *115*, B10414. https://doi.org/10.1029/2010JB007522

Lohman, R. B., & McGuire, J. J. (2007). Earthquake swarms driven by aseismic creep in the Salton Trough, California. *Journal of Geophysical Research*, *112*, B04405. https://doi.org/10.1029/2006JB004596

Lui, S. K., & Lapusta, N. (2016). Repeating microearthquake sequences interact predominantly through postseismic slip. *Nature Communications*, *7*, 13020. https://doi.org/10.1038/ncomms13020

Madariaga, R. (1979). On the relation between seismic moment and stress drop in the presence of stress and strength heterogeneity. *Journal of Geophysical Research*, *84*(B5), 2243–2250. https://doi.org/10.1029/JB084iB05p02243

Maeda, K. (1999). Time distribution of immediate foreshocks obtained by a stacking method. *Pure and Applied Geophysics*, *155*(2–4), 381–394.

Marone, C. (1998). Laboratory-derived friction laws and their application to seismic faulting. *Annual Review of Earth and Planetary Sciences*, *26*(1), 643–696. https://doi.org/10.1146/annurev.earth.26.1.643

Marone, C., & Kilgore, B. (1993). Scaling of the critical slip distance for seismic faulting with shear strain in fault zones. *Nature*, *362*(6421), 618–621. https://doi.org/10.1038/362618a0

Marone, C., Rayleigh, C. B., & Scholz, C. H. (1990). Frictional behavior and constitutive modeling of simulated fault gouge. *Journal of Geophysical Research*, *95*(B5), 7007–7025. https://doi.org/10.1029/JB095iB05p07007

McGuire, J. J., Boettcher, M. S., & Jordan, T. H. (2005). Foreshock sequences and short-term earthquake predictability on East Pacific Rise transform faults. *Nature*, *434*(7032), 457–461. https://doi.org/10.1038/nature03377

McLaskey, G. C., & Kilgore, B. D. (2013). Foreshocks during the nucleation of stick-slip instability. *Journal of Geophysical Research: Solid Earth*, *118*, 2982–2997. https://doi.org/10.1002/jgrb.50232

McLaskey, G. C., Kilgore, B. D., Lockner, D. A., & Beeler, N. M. (2014). Laboratory generated $M-6$ earthquakes. *Pure and Applied Geophysics*, *171*(10), 2601–2615. https://doi.org/10.1007/s00024-013-0772-9

Meier, M.-A., Heaton, T., & Clinton, J. (2016). Evidence for universal earthquake rupture initiation behavior. *Geophysical Research Letters*, *43*, 7991–7996. https://doi.org/10.1002/2016GL070081

Noda, H., Dunham, E. M., & Rice, J. R. (2009). Earthquake ruptures with thermal weakening and the operation of major faults at low overall stress levels. *Journal of Geophysical Research*, *114*, B07302. https://doi.org/10.1029/2008JB006143

Noda, H., & Lapusta, N. (2010). Three-dimensional earthquake sequence simulations with evolving temperature and pore pressure due to shear heating: Effect of heterogeneous hydraulic diffusivity. *Journal of Geophysical Research*, *115*, B12314. https://doi.org/10.1029/2010JB007780

Noda, H., & Lapusta, N. (2013). Stable creeping fault segments can become destructive as a result of dynamic weakening. *Nature*, *493*(7433), 518–521. https://doi.org/10.1038/nature11703

Noda, H., Lapusta, N., & Kanamori, H. (2013). Comparison of average stress drop measures for ruptures with heterogeneous stress change and implications for earthquake physics. *Geophysical Journal International*, *193*(3), 1691–1712. https://doi.org/10.1093/gji/ggt074

Peng, Z., & Gomberg, J. (2010). An integrated perspective of the continuum between earthquakes and slow-slip phenomena. *Nature Geoscience*, *3*(9), 599–607. https://doi.org/10.1038/ngeo940

Perfettini, H., & Avouac, J.-P. (2004). Postseismic relaxation driven by brittle creep: A possible mechanism to reconcile geodetic measurements and the decay rate of aftershocks, application to the Chi-Chi earthquake, Taiwan. *Journal of Geophysical Research*, *109*, B02304. https://doi.org/10.1029/2003JB002488

Perfettini, H., & Avouac, J.-P. (2007). Modeling afterslip and aftershocks following the 1992 Landers earthquake. *Journal of Geophysical Research*, *112*, B07409. https://doi.org/10.1029/2006JB004399

Reasenberg, P. A. (1999). Foreshock occurrence before large earthquakes. *Journal of Geophysical Research*, *104*(B3), 4755–4768. https://doi.org/10.1029/1998JB900089

Renard, F., Voisin, C., Marsan, D., & Schmittbuhl, J. (2006). High resolution 3D laser scanner measurements of a strike-slip fault quantify its morphological anisotropy at all scales. *Geophysical Research Letters*, *33*, L04305. https://doi.org/10.1029/2005GL025038

Rice, J. R. (1992). Fault stress states, pore pressure distributions, and the weakness of the San Andreas fault, *International geophysics* (vol. 51, pp. 475–503). Amsterdam, Netherlands: Elsevier. https://doi.org/10.1016/S0074-6142(08)62835-1

Rice, J. R. (1993). Spatio-temporal complexity of slip on a fault. *Journal of Geophysical Research*, *98*(B6), 9885–9907. https://doi.org/10.1029/93JB00191

Rice, J. R., Lapusta, N., & Ranjith, K. (2001). Rate and state dependent friction and the stability of sliding between elastically deformable solids. *Journal of the Mechanics and Physics of Solids*, *49*(9), 1865–1898. https://doi.org/10.1016/S0022-5096(01)00042-4

Rice, J., & Ruina, A. L. (1983). Stability of steady frictional slipping. *Journal of Applied Mechanics*, *50*(2), 343–349. https://doi.org/10.1115/1.3167042

Rubin, A., & Ampuero, J.-P. (2005). Earthquake nucleation on (aging) rate and state faults. *Journal of Geophysical Research*, *110*, B11312,. https://doi.org/10.1029/2005JB003686

Ruina, A. (1983). Slip instability and state variable friction laws. *Journal of Geophysical Research*, *88*(B12), 10,359–10,370. https://doi.org/10.1029/JB088iB12p10359

Sagy, A., Brodsky, E. E., & Axen, G. J. (2007). Evolution of fault-surface roughness with slip. *Geology*, *35*(3), 283–286. https://doi.org/10.1130/G23235A.1

Schaal, N. S. A. (2018). Modeling nucleation and dynamic rupture on heterogeneous frictional interfaces with applications to foreshocks (Ph.D. dissertation), California Institute of Technology. https://doi.org/10.7907/YCVJ-PM21

Schwartz, S. Y., & Rokosky, J. M. (2007). Slow slip events and seismic tremor at circum-Pacific subduction zones. *Reviews of Geophysics*, *45*, RG3004. https://doi.org/10.1029/2006RG000208

Segall, P., Desmarais, E. K., Shelly, D., Miklius, A., & Cervelli, P. (2006). Earthquakes triggered by silent slip events on Kīlauea volcano, Hawaii. *Nature*, *442*(7098), 71–74. https://doi.org/10.1038/nature04938

Segall, P., & Rice, J. R. (1995). Dilatancy, compaction, and slip instability of a fluid-infiltrated fault. *Journal of Geophysical Research*, *100*(B11), 22,155–22,171. https://doi.org/10.1029/95JB02403

Segall, P., Rubin, A. M., Bradley, A. M., & Rice, J. R. (2010). Dilatant strengthening as a mechanism for slow slip events. *Journal of Geophysical Research*, *115*, B12305. https://doi.org/10.1029/2010JB007449

Shelly, D. R., Beroza, G. C., & Ide, S. (2007). Non-volcanic tremor and low-frequency earthquake swarms. *Nature*, *446*(7133), 305–307. https://doi.org/10.1038/nature05666

Shelly, D. R., Beroza, G. C., Ide, S., & Nakamula, S. (2006). Low-frequency earthquakes in Shikoku, Japan, and their relationship to episodic tremor and slip. *Nature*, *442*(7099), 188–191. https://doi.org/10.1038/nature04931

Wei, S., Avouac, J.-P., Hudnut, K. W., Donnellan, A., Parker, J. W., Graves, R. W., et al. (2015). The 2012 Brawley swarm triggered by injection-induced aseismic slip. *Earth and Planetary Science Letters*, *422*, 115–125. https://doi.org/10.1016/j.epsl.2015.03.054

Zanzerkia, E. E., Beroza, G. C., & Vidale, J. E. (2003). Waveform analysis of the 1999 Hector Mine foreshock sequence. *Geophysical Research Letters*, *30*(8), 1429. https://doi.org/10.1029/2002GL016383

Zheng, G., & Rice, J. R. (1998). Conditions under which velocity-weakening friction allows a self-healing versus a cracklike mode of rupture. *Bulletin of the Seismological Society of America*, *88*(6), 1466–1483.